Title

Modelling Seasonal Ratcheting and Progressive Failure in Clay Slopes: A Validation

Authors

H. Postill MEng PhD
School of Architecture, Building and Civil Engineering, Loughborough University, Loughborough, UK
h.e.postill@lboro.ac.uk
ORCID 0000-0003-3157-718X

N. Dixon BSc PhD FGS
School of Architecture, Building and Civil Engineering, Loughborough University, Loughborough, UK
N.Dixon@lboro.ac.uk
ORCID 0000-0003-2995-0627

G. Fowmes EngD MSc BSc CEng MICE FHEA
School of Engineering, University of Warwick, UK
G.Fowmes@warwick.ac.uk
ORCID 0000-0002-5642-1109

A. El-Hamalawi BEng PhD MASCE MCGS FHEA PE
School of Architecture, Building and Civil Engineering, Loughborough University, Loughborough, UK
A.El-hamalawi@lboro.ac.uk

W. A. Take PhD PEng
Department of Civil Engineering, Queen's University, Kingston, Ontario, K7L 3N6, Canada
andy.take@queensu.ca
0000-0002-8634-1919

Corresponding author

Harry Postill
h.e.postill@lboro.ac.uk

Main Text Word Count: 7499
Number of Figures: 16
Number of Tables: 3

Date: 12th June 2019

Abstract

Seasonal wetting and drying stress cycles can lead to long-term deterioration of high-plasticity clay slopes through the accumulation of outward and downward deformations leading to plastic strain accumulation, progressive failure and first-time failures due to seasonal ratcheting. Using recent advances in hydro-mechanical coupling for the numerical modelling of unsaturated soil behaviour and development of nonlocal strain-softening regulatory models to reduce mesh dependency of localisation problems, the mechanism of seasonal ratcheting has been replicated within a numerical model. Hydrogeological and mechanical behaviours of the numerical model have been compared and validated against physical measurements of seasonal ratcheting from centrifuge experimentation. Following validation, the mechanism of seasonal ratcheting was explored in a parametric study investigating the role of stiffness and long-term behaviour of repeated stress cycling extrapolated to failure. Material stiffness has a controlling influence on the rate of strength deterioration for these slopes; the stiffer the material, the smaller the seasonal movement and therefore the more gradual the accumulation of irrecoverable strains and material softening. The validation presented provides confidence that the numerical modelling approach developed can capture near-surface behaviour of high-plasticity overconsolidated clay slopes subject to cyclic wetting and drying. The approach provides a tool to further investigate the effects of weather driven stress cycles and the implication of climate change on high-plasticity clay infrastructure slopes.

Key Words

Slope stability; Seasonal ratcheting; Progressive failure; Numerical modelling;

Nonlocal strain-softening

List of Notation

σ_B' = Bishop's generalised effective stress (kPa)
σ = total stress (kPa)
u_a = pore air pressure (kPa)
u_w = pore water pressure (kPa)
χ = is a parameter considering the area over which matric suction acts
s = matric suction (kPa)
S_r = degree of saturation
S_w = saturation
S_r^w = residual saturation
α = van Genuchten fitting parameter (kPa^{-1})
m = van Genuchten fitting parameter
K_{sat} = saturated hydraulic conductivity
K_r^w = relative hydraulic conductivity of water phase (m/s)
K_r^a = relative hydraulic conductivity of air phase (m/s)
ε_p^* = nonlocal plastic strain
V_w = weighted volume
ω' = is the weighting function
ε_d = local plastic strain
x_n = global coordinate
x_n' = local coordinate
l = internal length
r = distance from the stress point to adjacent stress points
K = bulk modulus (kPa)
G = shear modulus (kPa)
v = specific volume
κ = gradient of the swelling line
λ = gradient of normal consolidation line
σ_{ref} = reference pressure (kPa)
v_κ = specific volume at reference pressure following the swelling line
v_λ = original specific volume at reference pressure
v' = Poisson's ratio
e = void ratio
$k_{sat,vertical}$ = vertical saturated hydraulic conductivity (m/s)
$k_{sat,horizontal}$ = horizontal saturated hydraulic conductivity (m/s)
OCR = overconsolidation ratio
K_0 = coefficient of earth pressure at rest
K_{nc} = coefficient of earth pressure at rest normally consolidated
c' = cohesion (kPa)
φ' = internal angle of friction (°)

Introduction

Long-term deterioration of high-plasticity clay slopes due to seasonal wetting and drying induced pore water pressure fluctuations driving effective stress cycles, has been attributed as the cause of shallow (i.e. less than 2.5m deep) first-time failures in clay infrastructure slopes (Take & Bolton, 2011; Briggs, et al., 2017). Within this study, pore water pressure fluctuations and resulting effective stress cycles due to environmental boundary conditions are referred to as environmental stress cycles. These environmental cycles of wetting and drying cause cyclic volume change that can lead to the accumulation of irrecoverable plastic strains resulting in mobilisation of post-peak strength and progressive failure (Take, 2003; Take & Bolton, 2004; Take & Bolton, 2011). This mechanism of shallow first-time failure due to repeated environmental stress cycles and progressive failure, known as seasonal ratcheting (Take & Bolton, 2011), has been observed in high-plasticity clay rail infrastructure slopes (Briggs, et al., 2017), and was shown conclusively through centrifuge experimentation (Take & Bolton, 2011). The mechanism of seasonal ratcheting in high-plasticity clay slopes is the focus of the study reported in this paper. While seasonal movement due to environmental wetting and drying stress cycles has been shown to occur in intermediate-plasticity clay slopes (Hudacsek, et al., 2009), progressive failure was not observed within this centrifuge experimentation. The reasons for this were highlighted as a difference in stress history (i.e. Take and Bolton (2011) considered overconsolidated high-plasticity clay and Hudacseck, et al., (2009) intermediate-plasticity compacted clay fill) as well as the difference in mechanical properties of the high and intermediate-plasticity materials investigated (Hudacsek, et al., 2009).

Environmental stress cycles in high-plasticity clay slopes, due to wetting and drying, and progressive failure have been investigated through numerical analyses providing useful parametric studies to develop understanding of the mechanism (Kovacevic, et al., 2001; Nyambayo, et al., 2004; O'Brien, et al., 2004; Tsiampousi, et al., 2017). It has been shown that hydraulic conductivity (Nyambayo, et al., 2004) and vegetation (O'Brien, et al., 2004; Tsiampousi, et al., 2017) significantly influence the rate of failure of high-plasticity clay slopes driven by cycles of effective stresses that result from cyclic environmental boundary conditions. Within these studies, the failure surfaces obtained are deep-seated (i.e. greater than 2.5m deep) and behaviour modelled as fully saturated. While the studies are valuable, they do not adequately capture seasonal ratcheting and shallow first-time failures. In particular, the nature and magnitude of shrink-swell cycles leading to outward and downward movements, plastic strain accumulation leading to progressive failure, have not been captured in numerical models presented by Kovacevic, et al., (2001), Nayambayo, et al., (2004), O'Brien, et al., (2004) and Tsiampousi, et al., (2017). Therefore, additional work is required to model the mechanism of seasonal ratcheting to allow further development in understanding of the mechanism and to investigate the implications of changing seasonal weather patterns in the future due to climate change.

Recently, sophisticated soil-vegetation-atmosphere boundary conditions that drive representative hydrogeological behaviour of slopes within numerical models have been developed to investigate time dependent slope behaviour (Rouainia, et al., 2009; Conte, et al., 2016; Elia, et al., 2017). In the work by Conte, et al., (2016) and cases considered by Elia, et al., (2017), coupled hydro-mechanical numerical analyses validated against monitored data have shown good agreement for displacements driven by changing pore water pressures resulting from

environmental boundary cycles for reactive landslides (i.e. movements along defined existing shear surfaces, where material is already at or near residual strength, therefore strain-softening is not considered within this previous work). Whilst the modelling approaches show that environmental stress cycles due to weather sequences can be replicated numerically, the Conte, et al., (2016) model and models discussed by Elia, et al., (2017) did not consider the accumulation of plastic strains and progressive failure due to these stress cycles (i.e. the work is not explicitly considering seasonal ratcheting). Therefore, additional work is required for more complex strain-softening problems such as seasonal ratcheting in high-plasticity clay slopes.

As seasonal ratcheting drives progressive failure, strain-softening behaviour must be included within the modelling. It is known that localisation problems within discretised numerical analyses suffer mesh dependency (Galavi & Schweiger, 2010; Summersgill, et al., 2017). Recent advances in nonlocal strain-softening regulatory models have been shown to significantly reduce mesh dependency of such problems (Summersgill, et al., 2017).

This paper presents a coupled hydro-mechanical unsaturated (i.e. a soil containing both a liquid and a gas phase) numerical model capable of modelling seasonal ratcheting movements due to known environmental stress cycles. This work does not consider or develop current knowledge of soil-vegetation-atmosphere boundary conditions but focusses on the consequences of cyclic stress changes due to pore water pressure fluctuations within high-plasticity overconsolidated clay slopes causing seasonal ratcheting leading to shallow first-time progressive failure. It purposefully does not consider deep-seated mechanisms that have been the focus of other studies (e.g. Potts, et al., 1997). The focus of this study is justified because

shallow first-time failure in high-plasticity clay slopes is particularly important in the assessment of long-term behaviour of infrastructure earthwork assets (Briggs, et al., 2017).

This work is differentiated from previous studies considering seasonal environmental stress cycles and progressive failure by the level of validation conducted through direct comparison of numerical analyses against physical modelling data presented by Take and Bolton (2011). The numerical model developed includes unsaturated behaviour and a nonlocal strain-softening regulatory model has been implemented to reduce mesh dependency for the modelling of progressive failure.

Physical Modelling

Physical models provide controlled conditions limiting unknowns and therefore they can be used to assess validity of assumptions required for the development of a numerical model that can replicate measured behaviour. In addition, materials used in physical models have known properties, the stress history is controlled and boundary conditions are well established. The physical modelling conducted by Take (2003) and presented by Take and Bolton (2011) provides pore water pressure (i.e. hydrogeological) and displacement (i.e. mechanical) data for Kaolin slopes subject to repeated simplified environmental stress cycles due to wetting and drying.

This paper focuses on two tests considering Speswhite Kaolin with a slope inclination of 36 degrees, models WAT7a and WAT8a (Take & Bolton, 2011). The slopes were 140mm high at 1/60th scale with tests run under centripetal acceleration of 60g, corresponding to a slope height of 8.4m at full scale. The only differences between the two models are the pressure under which the initial Kaolin blocks were

consolidated and the magnitude and timing of wetting and drying boundary conditions applied.

The slope models were formed through the following steps as described by Take (2003) and Take and Bolton (2011). Speswhite Kaolin was mixed to 120% moisture content and subjected to one-dimensional consolidation within a consolidometer to form an initial block. Loading was used to increase the vertical stresses within the consolidometer as follows for WAT7a: 2, 10, 15, 30, 60, 120, 250 and 500kPa, and for WAT8a the same stress path was followed but a maximum vertical stress of 200kPa applied. After application of each load increment, primary consolidation was allowed prior to the next load increase. Unloading was done in 75 kPa increments and swelling was allowed to occur. Following consolidation and subsequent swelling, the slope models were formed (Take & Bolton, 2011).

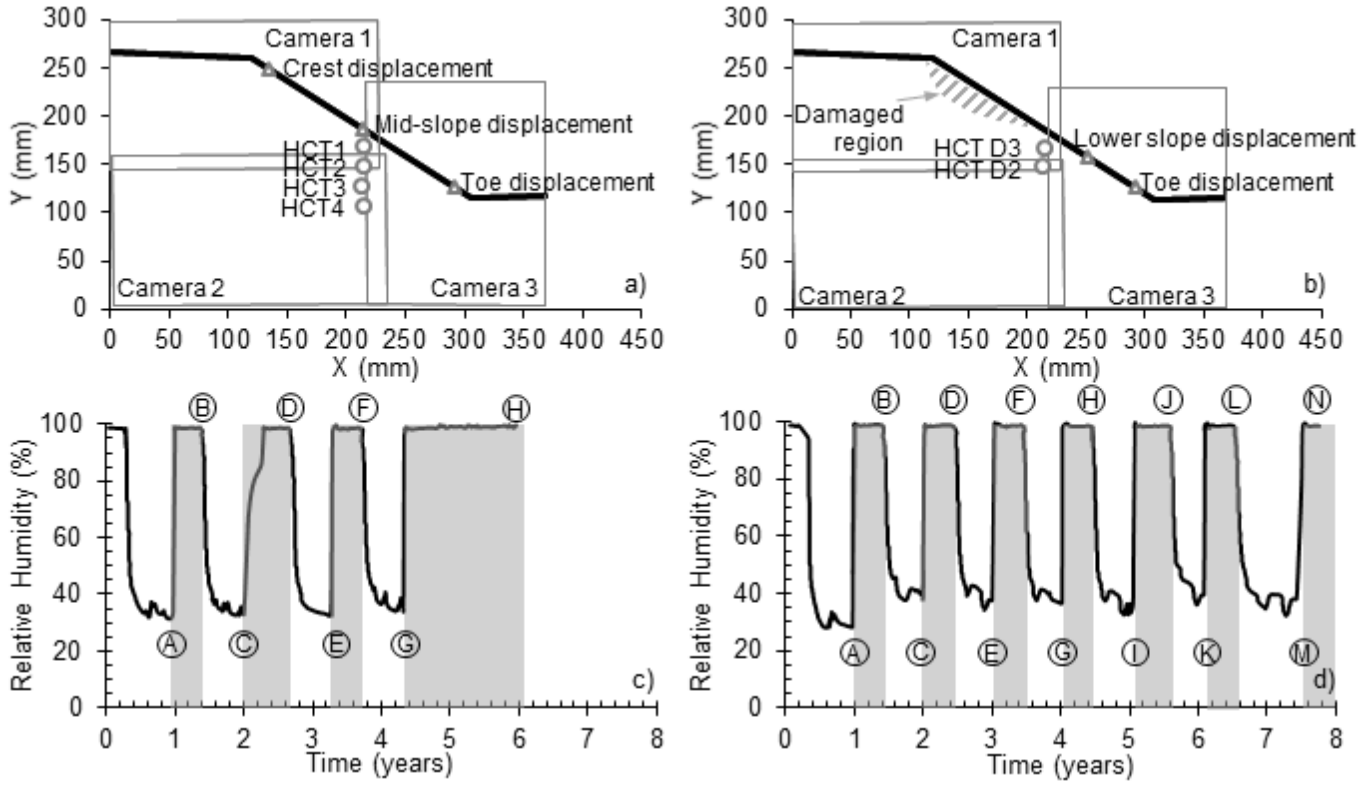

Figure 1 shows the geometry and location of monitoring equipment for the two physical model experiments, camera locations for displacement measurements through particle image velocimetry (PIV) (White, et al., 2003) and high-capacity tensiometer (HCT) (Take & Bolton, 2003) locations for pore water pressure measurements.

Boundary conditions were controlled using a climate chamber developed by Take and Bolton (2002). Simulated rainfall, using suspended misting nozzles, and a relative humidity of 100% were used to replicate wet winter conditions and relative humidity of approximately 40% without simulated rainfall used to replicate dry summer conditions. The boundary conditions applied are shown in

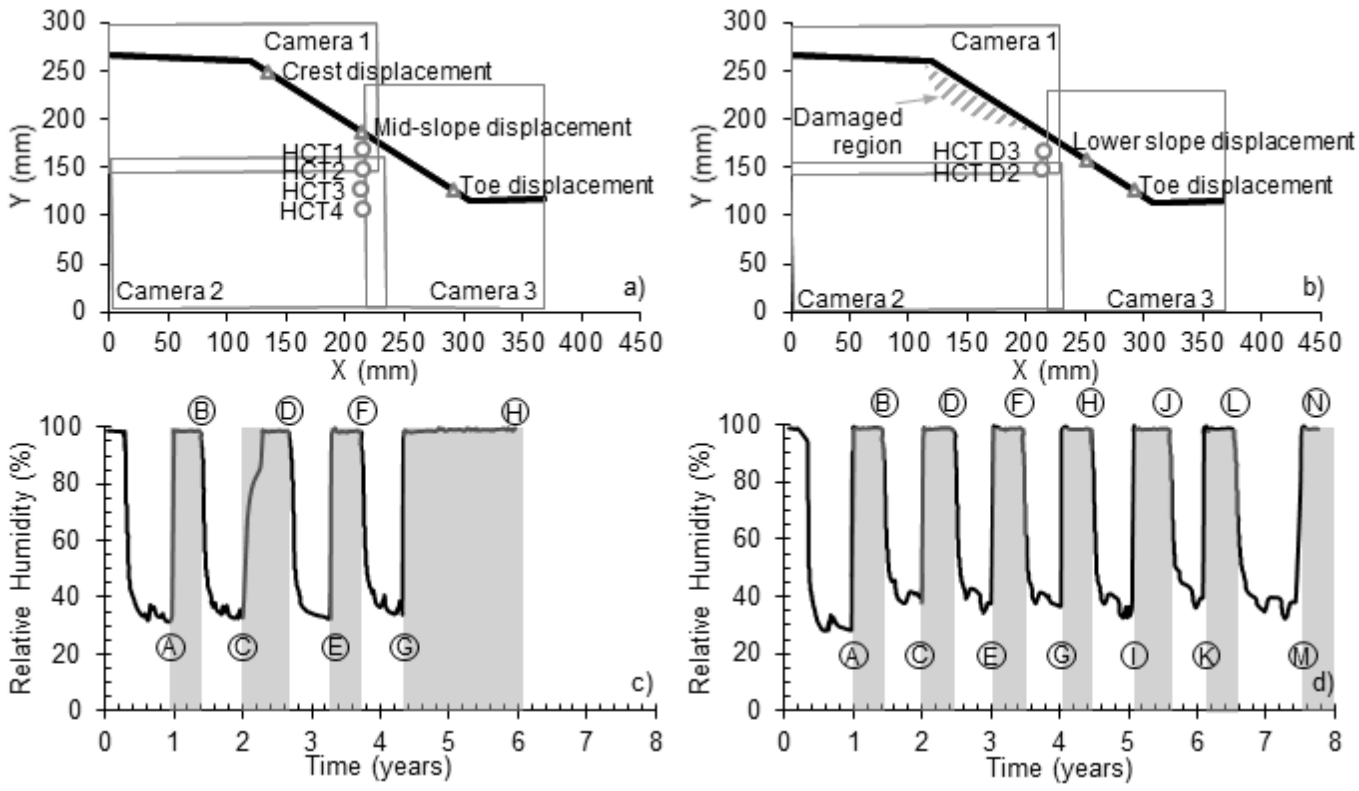

Figure 1; the grey regions indicate the use of the mist nozzles. For WAT7a, four seasonal cycles were applied and then the model was subjected to prolonged wetting (G to H). WAT8a was subjected to seven seasonal cycles. In both instances

strain-softening was observed and small localised failures at the toe of the slopes occurred.

Take and Bolton (2011) concluded that seasonal variation in soil water content drive stress changes within slopes that can, in some cases, mobilise post-peak strength at which point irrecoverable strain accumulation and softening occurs. Results from the physical modelling are presented alongside numerical analyses results throughout this paper.

Numerical Modelling Framework

Shallow first-time failure of a clay slope due to seasonal ratcheting is driven by pore water pressure variation due to cycles of wetting and drying, which includes unsaturated soil behaviour. Near surface desaturation as a result of environmental boundary conditions has been observed in high-plasticity clay slopes (Smethurst, et al., 2006; Smethurst, et al., 2012), and is a significant factor in slope behaviour. Soil water content variation changes pore water pressures, affecting relative hydraulic conductivity and internal stress conditions; which in turn influence the strength, stiffness and volume of a soil. These behaviours are inter-related and must be accounted for in any numerical modelling approach.

Unsaturated soil behaviour can be modelled by coupling hydrogeological (i.e. the movement of water through a soil mass) and mechanical behaviour. Within this paper, mechanical behaviour is described using Bishop's generalised effective stress and coupled with hydrogeological behaviour through the addition of hydrogeological descriptors, matric suction and degree of saturation allowing stresses to be determined and flow of air and water phases through the soil to be established.

Bishop's generalised effective stress is a single stress state variable that combines multiple stresses (σ, u_w, u_a) from a multi-phase medium (soil, water and air) into one variable that can be used to describe physical behaviour. This is given in Equation (1).

$$\sigma'_B = (\sigma - u_a) + \chi(u_a - u_w)$$

Equation (1)

Where, σ'_B = Bishop's generalised effective stress; σ = total stress; u_a = pore air pressure; u_w = pore water pressure; $(\sigma - u_a)$ = net stress; $s = (u_a - u_w)$ = matric suction; χ = is a parameter considering the area over which matric suction acts (1 being fully saturated and 0 being dry).

Within this work, it is assumed that χ is equivalent to the degree of saturation. This has been shown to be an approximation and the parameter is different for all soils depending on their microstructure (Jardine, et al., 2004). However, the single effective stress variable allows easy transition between saturated and unsaturated behaviour and can account for shear strength variation effectively, which is the critical variable for slope stability analysis. Whilst this framework can capture shear strength variation well, it should be noted that it is currently not possible for all unsaturated mechanical behaviours, in particular wetting collapse, to be accounted for using a single stress state variable (Jardine, et al., 2004; Nuth & Laloui, 2008).

The hydrogeological component of the framework links soil water content and matric suction through a soil water retention curve. Within this work, a van Genuchten (1980) style soil water retention curve has been used, see Equation (2). The resulting suction and degree of saturation are then used along with the saturated

hydraulic conductivity to establish the relative hydraulic conductivity of the water and air phases. Equations for relative hydraulic conductivity are shown in Equation (3) for the water phase and Equation (4) for the air phase (van Genuchten, 1980). The flow of the two phases within the soil are calculated using Darcy's law, taking into account the viscosity of the different phases. Within the framework, it is assumed that the water and air phases are idealised and homogeneous (i.e. air is not dissolved into the water phase resulting in pure water and air components).

$$s = \alpha\left[S_r^{-1/m} - 1\right]^{1-m}$$

Equation (2)

Where, s = matric suction; $S_r = \frac{S_w - S_r^w}{1 - S_r^w}$ = degree of saturation; S_w = saturation; S_r^w = residual saturation; α = van Genuchten fitting parameter (kPa^{-1}); and m = van Genuchten fitting parameter.

$$K_r^w = K_{sat}.S_r^{0.5}\left[1 - (1 - S_r^{1/m})^m\right]^2$$

Equation (3)

$$K_r^a = K_{sat}.(1 - S_r)^{0.5}\left[1 - S_r^{1/m}\right]^{2m}$$

Equation (4)

Where, K_r^w = relative hydraulic conductivity of water phase (m/s); K_r^a = relative hydraulic conductivity of air phase (m/s); and K_{sat} = saturated hydraulic conductivity (m/s).

Using degree of saturation within Bishop's generalised effective stress and within the soil water retention curve, hydrogeological and mechanical behaviours have been

coupled within this framework. This framework has been adopted within many commercially available numerical modelling software packages and the advantages of this framework have been discussed by Nuth and Laloui (2008).

A Mohr-Coulomb strain-softening constitutive model with material softening and non-associated shear flow rule has been used in this study. This constitutive model has been adopted to allow post-peak strain softening to be modelled effectively (Potts, et al., 1990; Potts, et al., 1997), a critical behaviour of seasonal ratcheting leading to first-time failure due to repeated environmental stress cycles (Rouainia, et al., 2009; Take & Bolton, 2011). Considering the stresses obtained using Equation (1), and yield surface defined by the Mohr-Coulomb constitutive model, elastic and plastic strains are determined. To reduce mesh dependency due to localisation, a nonlocal strain-softening model has been implemented. The modelling undertaken within this work has been carried out in the explicit finite difference modelling code, FLAC – Two-Phase Flow option (FLAC-TP) (Itasca, 2011).

Implementation of Nonlocal Strain-Softening Model

A partial nonlocal strain-softening model has been implemented, with local plastic strains averaged relative to each stress point within the mesh using a weighting function to obtain the nonlocal plastic strain value (Galavi & Schweiger, 2010; Summersgill, et al., 2017). Nonlocal plastic strains are calculated at each time-step and dictate material softening. The implementation procedure adopted is similar to that described by Galavi and Schweiger, (2010); however, a Mohr-Coulomb strain-softening constitutive model with material softening, to allow progressive failure to be modelled, has been employed. The nonlocal plastic strain (ε_p^*) at stress point (x_n) is calculated using Equation (5).

214 $$\varepsilon_p^*(x_n) = \frac{1}{V_w}\iiint \omega'(x_n')\varepsilon_d(x_n + x_n')dx_1'dx_2'dx_3'$$

215 Equation (5)

216 Where, $V_w = \iiint \omega(x_n')\, dx_1'dx_2'dx_3'$ = weighted volume; $\omega'(x_n')$ = is the weighting
217 function; $\varepsilon_d(x_n + x_n')$ = local plastic strain at different calculation points; x_n = global
218 coordinate; x_n' = local coordinate.

219 The weighting function adopted in the current work takes the form of the distribution
220 proposed by Galavi and Schweiger (2010) and is given in Equation (6); the centre of
221 the weighting function is located at the stress point at which the nonlocal plastic
222 strain is being calculated. Summersgill (2015) showed that for numerical models of
223 cut slopes, the weighting function proposed by Galavi and Schweiger (2010)
224 produces results that are the least mesh-dependent compared to alternative
225 weighting functions such as the gaussian distribution used by Bažant, et al., (1984)
226 or the over-nonlocal method used by Vermeer and Brinkgreve (1994).

227 $$\omega'(r) = \frac{r}{l}e^{-(\frac{r}{l})^2}$$

228 Equation (6)

229 Where, l = internal length and r = distance from the stress point to adjacent stress
230 points.

231 As mesh dependency of local and nonlocal strain-softening models and the effect of
232 different weighting functions have been rigorously examined by Summersgill, et al.,
233 (2017), the work reported in this paper utilises the nonlocal strain-softening
234 regulatory approach but does not aim to further advance current methodology.

Mechanical Properties

As discussed previously, seasonal ratcheting can lead to mobilisation of post-peak strength and progressive failure. Therefore, establishing the correct strain-softening model, strength, strains, and stiffness relationship is fundamental for the correct modelling of the behaviour being investigated. The relationships for material parameters used within the slope analyses have been taken from literature and derived through the calibration of single element numerical analysis of overconsolidated drained triaxial tests against experimental data for Kaolin. Take and Bolton (2011) used Speswhite Kaolin within their centrifuge experimentation under the rational that the material has been well classified by others within the literature.

Stiffness Properties

The stiffness relationships adopted for Kaolin have been taken from reported numerical modelling of a Kaolin embankment centrifuge experiment (Almeida, et al., 1986) in which the bulk and shear moduli are a function of the specific volume, mean effective stress and are updated at each time-step (Schofield & Wroth, 1968). Small-strain stiffness, which is known to influence the rate of plastic strain accumulation and non-linearity of stiffness, has been omitted from this study as deformations observed in the physical modelling are far in excess of small-strain criteria (i.e. >1% strain). Therefore, the use of a stress-dependent stiffness model based on large-strain stiffness, which has been used in previous numerical modelling of a Kaolin embankment in centrifuge experimentation (Almeida, et al., 1986), is more appropriately aligned to the stain conditions being modelled. The additional computational requirements to include small-strain stiffness is not merited for the negligible impact this will have on model results.

$$K = \frac{v.\sigma'}{\kappa} \; ; \min 2000kPa$$

Equation (7)

$$G = \frac{3(1-2v')}{2(1+v')}.K$$

Equation (8)

Where, K = bulk modulus (kPa); G = shear modulus (kPa); v = specific volume ($v = 1 + e$); e = void ratio; κ = gradient of the swelling line; v' = Poisson's ratio and σ' = mean effective stress (kPa) (Bishop's generalised effective stress).

Specific volume is obtained from knowledge of the consolidation and swelling properties, the stress history, and the current stress state of the soil (Schofield & Wroth, 1968). The specific volume, and thus stiffness, of the soil will change due to cycles of wetting and drying, driving pore water pressure cycles that act as environmental loading and unloading changing the effective stress state of the soil. This can be considered in the $v: \ln(\sigma')$ space in line with Equation (9) and Equation (10).

$$v = v_\lambda - \lambda.ln\frac{\sigma'}{\sigma_{ref}}, \text{normal consolidation line}$$

Equation (9)

$$v = v_\kappa - \kappa.ln\frac{\sigma'}{\sigma_{ref}}, \text{swelling lines}$$

Equation (10)

Where; λ = gradient of the virgin compression line; σ_{ref} = reference pressure (kPa); v_λ = original specific volume at reference pressure; v_κ = specific volume at reference pressure following the swelling line.

For Kaolin, the gradient of the normal consolidation line can be taken as $\lambda = 0.25$ and the swelling line as $\kappa = 0.05$ (Clegg, 1981; Take, 2003). Kaolin consolidated to 500kPa is cited as having a void ratio of approximately $e = 1.0$ (Al-Tabbaa & Wood, 1987). The corresponding specific volume at 500kPa is therefore $v = 2.0$ and the specific volume for a reference pressure of 1kPa is $v_\lambda = 3.55$.

Strength Properties

To calibrate the strength and plastic strain criteria for the strain-softening behaviour of Kaolin, an axisymmetric single element numerical model employing a local strain-softening model was used to replicate drained overconsolidated triaxial tests (note that the nonlocal strain-softening regulatory model cannot be used for a single element model as no averaging of local strains can occur). For the slope analyses, the local plastic strain criteria obtained from the numerical analyses of the triaxial tests (i.e. $\varepsilon_{d,peak}$ = 0.05 and $\varepsilon_{d,critical\_state}$ = 0.15) have been adopted within the nonlocal strain-softening model (i.e. $\varepsilon^*_{p,peak}$ = 0.05 and $\varepsilon^*_{p,critical\_state}$ = 0.15) along with an internal length parameter equivalent to element thickness. This follows the method presented by Summergill, et al., (2017) where local plastic strain criteria from previous studies have been taken as the nonlocal plastic strain criteria for analysis of London Clay cut slopes.

The dilation angle used in the numerical analyses has been assumed to be ψ = 0, as dilation only affects the thickness of the shear surface, which is not critical in the current study, not the magnitude of shear strains along the shear surface.

Mechanical Behaviour

An axisymmetric, single element numerical model of overconsolidated drained triaxial tests has been conducted to replicate tests undertaken by Cekerevac and Laloui (2004). The model was fully saturated, and volume change due to drainage was permitted (i.e. drained conditions were maintained). The samples were initially consolidated to 600kPa and then unloaded to 100kPa (OCR=6) and 50kPa (OCR=12). The initial stresses were applied to the numerical model and the horizontal confining pressure fixed. A constant velocity was applied to the top of the element to emulate loading in a strain-controlled test. The specific volume relationship for the triaxial test numerical model is dependent on the swelling line following the consolidation to 600kPa, giving $v_{\kappa,ref} = 2.27$ at a reference pressure of 1kPa. The stress path of the samples and corresponding specific volume can be seen in Figure 2a. During the analysis, the deviator stress, axial strain and stress path of the model were monitored; these have been compared against experimental data for Kaolin presented by Cekerevac and Laloui (2004) in Figure 2.

Figure 2b shows that the peak strength mobilised for different overconsolidation ratios in the numerical model are of comparable magnitudes and mobilised at axial strains representative of the experimental triaxial tests. This good fit confirms the relevance of the strength parameters, the strain criteria, and the stiffness relationship adopted for the mechanical behaviour of Kaolin. Importantly, the numerical model captures the softening behaviour from peak to critical state at large strains, omitting this mechanism from the numerical analyses has significant implications as post-peak strength cannot be mobilised, a mechanism that is fundamental to this study.

To assess the significance of the strain-softening model and stiffness relationship presented, simple sensitivity analyses where these mechanisms were omitted for the same triaxial test models were conducted, these are shown within

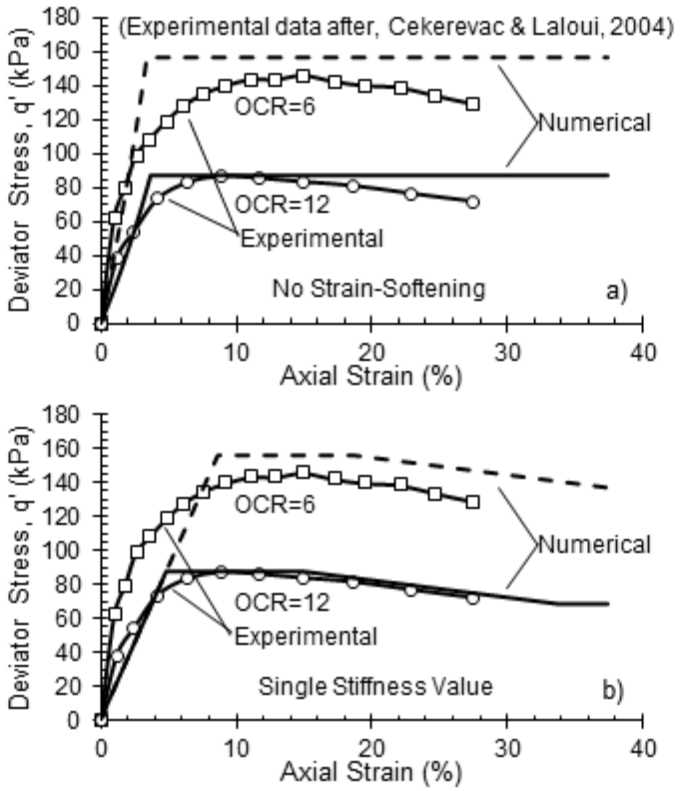

Figure 3. Without strain-softening behaviour, post-peak strength is not modelled, and strength at large strains is grossly overestimated, see

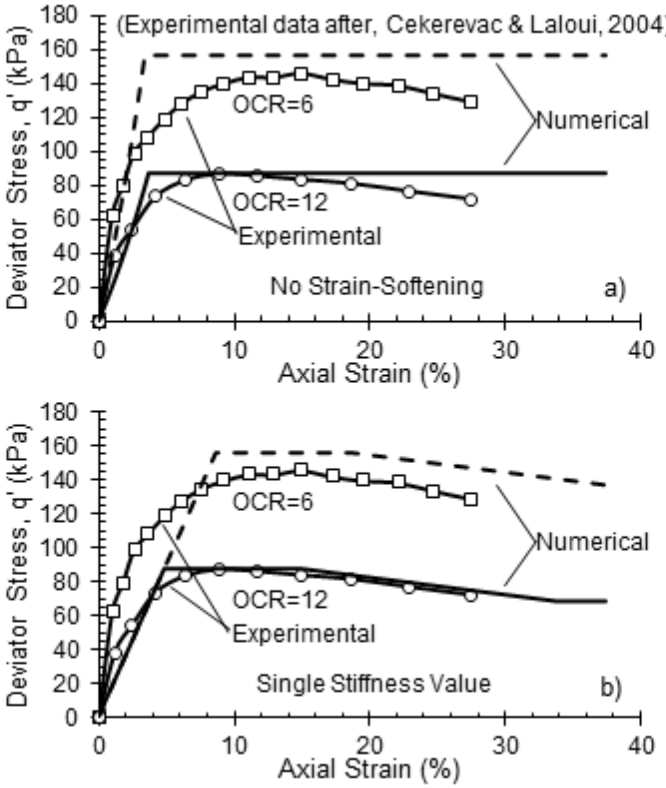

330 Figure 3a. Without stiffness related to specific volume (i.e. single value of bulk and
331 shear moduli), there is a significant difference in the strains at which peak strength
332 are mobilised and the difference in the stress history (i.e. the overconsolidation ratio)
333 of the samples is not accounted for, see

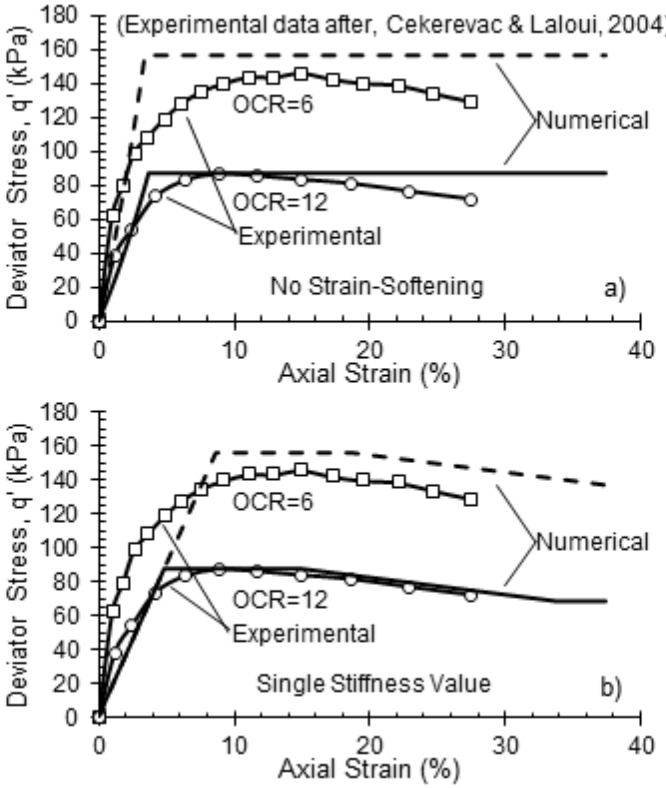

Figure 3b. The derived strain-softening parameters, plastic strain criteria and other mechanical properties used in the numerical analyses of the slope models are summarised in Table 1.

Hydrogeological Properties

To complete the coupled hydro-mechanical framework, soil water retention properties for Kaolin are presented in Figure 4 and summarised in Table 2. Soil water retention properties have been derived by fitting a van Genuchten (1980) style soil water retention curve to experimental data from Tarantino (2009), Hu, *et al*., (2013) and Tripathy, *et al*., (2014). The soil water retention curve used in this work does not account for hysteresis effects due to wetting and drying, which have been shown to be important in modelling infiltration (Bashir, et al., 2016), or the fact that soil water retention properties vary with void ratio (Hu, et al., 2013). In addition, the effect of deterioration of soil water retention properties due to repeated stress cycles

has not been accounted for. These simplifications have been made as the magnitude of pore water pressure variation is relatively small and only a small number of wetting and drying cycles are experienced. Therefore, the effect of hysteresis and soil water retention property deterioration on the model results will be small. As stated previously, this work looks to validate mechanical behaviour due to established environmental stress cycles, so as long as hydrogeological behaviour, and corresponding stress cycles, can be suitably replicated this simplification of soil water retention properties is considered acceptable.

When modelling complex stratigraphy, it has been shown that including depth dependent saturated hydraulic conductivity is important (Potts, et al., 1997). Within this exercise, prior to the seasonal wetting and drying cycles, the Kaolin block has been consolidated to a near constant void ratio and therefore has a uniform saturated hydraulic conductivity at initialisation of the model. Some variability will occur in saturated hydraulic conductivity due to swelling during wetting and shrinkage due to drying and this is accounted for by the saturated hydraulic conductivity being void ratio, and therefore stress, dependent. The relationships used to calculate saturated hydraulic conductivity are empirical and taken from laboratory studies of Kaolin by Al-Tabbaa and Wood (1987). The saturated hydraulic conductivity relationship is given in Equation (11) and Equation (12), in which the vertical and horizontal saturated hydraulic conductivity are related to void ratio ($e = v - 1$) and are updated at each time-step within the numerical model; void ratio is calculated considering specific volume as presented previously for the stiffness relationship. This relationship has been included to allow the saturated hydraulic conductivity to change depending on the stress state of the soil. Figure 4b shows the effect of different void ratios on the relative hydraulic conductivity function, calculated

in line with the closed form solution presented by van Genuchten (1980), for water within the soil. As the void ratio increases (i.e. stresses reduce), the saturated hydraulic conductivity and therefore relative hydraulic conductivity increases.

$$k_{sat,vertical} = 0.53e^{3.16} \times 10^{-9}\ m/s$$

Equation (11)

$$k_{sat,horizontal} = 1.49e^{2.03} \times 10^{-9}\ m/s$$

Equation (12)

Validation of the Numerical Modelling Approach

Using the material parameters and relationships presented, a comparison of hydrogeological and mechanical response of the two 1/60th 60g physical models described previously (Take, 2003; Take & Bolton, 2011), with full scale 1g numerical analyses has been conducted. All times and displacements from the physical modelling have been scaled to full scale 1g; scaling factors from centrifuge ng to full scale 1g are time, n^2 and length, n.

The hydrogeological response of the numerical analyses and boundary conditions applied have been compared with pore water pressure measurements from high-capacity tensiometers in the physical modelling (Take & Bolton, 2003). The mechanical responses of the numerical analyses are compared with displacements obtained from the physical modelling using the PIV measurement technique (White, et al., 2003).

Initial Conditions

To replicate the steps taken to initiate the physical model by Take (2003), in the numerical model Kaolin blocks were initially saturated and subjected to one-dimensional consolidation to 500kPa (WAT7a) and 200kPa (WAT8a) and unloaded to 0kPa. Complete pore water pressure equilibration was reached between each loading increment within the numerical analyses. In the physical modelling, the slope was shaped in the block of consolidated material at 1g, then spun to equilibrium at 60g in the centrifuge. To replicate this in the numerical analysis, following the one-dimensional consolidation, the horizontal stresses were initiated to replicate the stress history of the material in the physical models and then the slope formed through the removal of elements.

Horizontal stresses, initiated within the Kaolin block following one-dimensional consolidation, have been determined by considering the overconsolidation ratio and the coefficient of earth pressure at rest (K_0) of the physical models. The overconsolidation ratio was determined using Equation (13). The coefficient of earth pressure at rest for reconstituted clays has been shown to fit the empirical relationship given in Equation (14) (Mayne & Kulhawy, 1982).

$$OCR = {\sigma'_{v,maximum}}\Big/{\sigma'_{v,current}}$$

Equation (13)

$$K_0 = K_{nc}.(OCR)^{\varphi'}$$

Equation (14)

Where; $K_{nc} = 1 - \sin\varphi'$ and φ' is in radians in Equation (14).

The overconsolidation ratio, coefficient of earth pressure at rest, vertical and horizontal stress with depth for both WAT7a and WAT8a are shown in Figure 5 for conditions prior to shaping of the slope profile.

The physical models considered by Take (2003) and Take and Bolton (2011) were 260mm high and the nominal radius of the centrifuge used at the University of Cambridge is 4.125m (Wood, 2004). As the model height is less than 0.1 times the radius of the centrifuge arm, the variation in the centripetal acceleration across the depth of the sample can be assumed to be negligible (Wood, 2004) and has therefore been omitted from the numerical model.

As with the triaxial test, the specific volume of the soil must be considered within the numerical model to ensure mechanical and hydrogeological behaviour is being captured correctly. The specific volume relationships for the two slope models are shown in Figure 6, where $v_{\kappa,500} = 2.31$ and $v_{\kappa,200} = 2.49$. As stresses within the slope due to seasonal boundary conditions do not exceed the original consolidation pressures of either slope model, further movement along the virgin compression line will not occur.

It should be noted that during formation of the physical model WAT8a, the region near the crest of the slope was damaged and a portion of the slope became dislodged during the initial seasonal cycle before reattaching during a drying phase. The portion affected is shown in

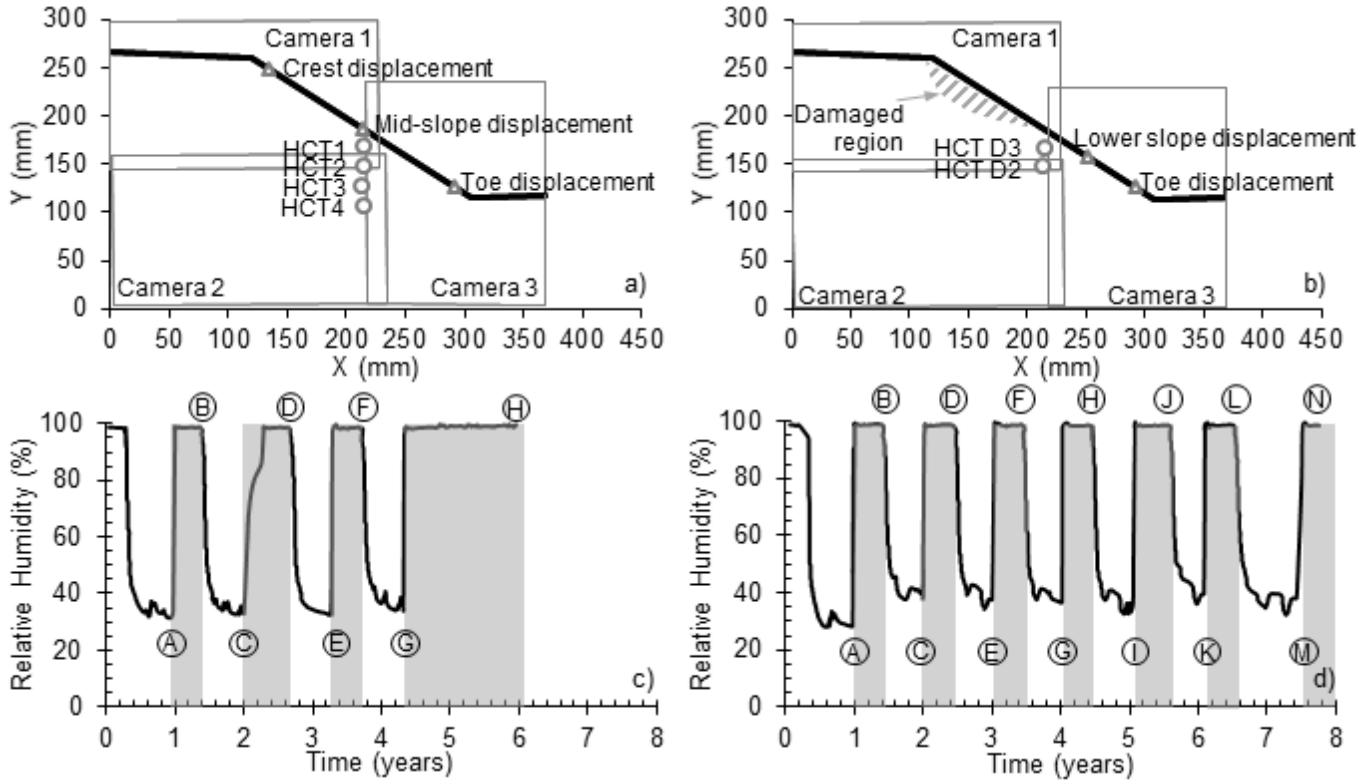

Figure 1. To ensure that this event does not influence the comparison of mechanical behaviour between the physical and numerical models, displacement records are considered only at the lower part and toe of the slope for model WAT8a.

Boundary Conditions

To replicate transient pore pressure conditions, and therefore environmental stress cycles, generated during the physical modelling, the numerical models have been subjected to inflow and outflow discharge boundary conditions along the model upper surface (i.e. toe, slope and crest).

During the physical modelling, it was not possible to determine the exact quantity of water flowing into and out of the slope. Therefore, the numerical model discharge boundary conditions have been applied to drive the pore pressure cycles observed at HCT1 for WAT7a and HCT D3 for WAT8a, and hence produce the environmental stress cycles in the near-surface of the slope of the same magnitude and frequency

447 to those observed in the physical model. For completeness, the discharges applied
448 to the slope surface are presented in Figure 8. The tensiometers used to measure
449 pore water pressures are approximately 1.0m below the slope surface at full scale
450 and are the closest measurements of hydrogeological behaviour to the slope surface
451 where the boundary conditions are applied; the implications of this are discussed
452 later. It should be noted that during drying, pore water pressure suctions along the
453 slope surface to achieve the correct suctions in HCT1 and HCT D3, were much
454 higher than at the location of HCT1 and HCT D3 resulting in the near-surface of the
455 slope becoming desaturated within the numerical analyses. A typical mesh of 0.5 x
456 0.5m elements used for the numerical modelling is shown in Figure 7.

457 The work presented here does not further current modelling capabilities to assess
458 soil-vegetation-atmosphere interactions but aims to validate mechanical behaviour of
459 seasonal ratcheting and accumulated deterioration due to the imposed wetting and
460 drying stress cycles.

461 ***Hydrogeological Response***

462 Figures 9 and 10 show the magnitude and timings of maximum and minimum
463 seasonal pore water pressure cycles are comparable between the experimental and
464 numerical models. The near-surface pore water pressures driving stress changes in
465 the main area of interest (i.e. the near-surface) are a close match. It should be noted
466 that for WAT7a, at waypoint C, the centrifuge was temporarily paused to allow
467 cameras to be reset and as such the dip in pore water pressures at this point are an
468 artefact of this process and have not be replicated within the numerical model,
469 therefore, the focus is waypoint D onwards. The drying phase within the numerical
470 modelling captures the same hydrogeological behaviour as that of the physical

model. However, the numerical model does not perform as well during the wetting phase. This can be explained by the fact that the numerical models assume the material is uniform whereas in reality, preferential flow routes exist as well as gaps between the slope and the centrifuge chamber following drying, causing shrinkage of the clay. This led to an increased hydraulic conductivity following the change in boundary conditions from drying to wetting that cannot be accounted for within the numerical analysis.

Figures 9 and 10 show that the stress path taken by elements of soil during wetting differs between the numerical and physical modelling, however, the stress state (i.e. pore water pressures) within the different analyses are equivalent at each waypoint (i.e. point of change between wetting or drying); both the physical and numerical models reach the same conditions at the same time for the maximum and minimum values in each cycle. Therefore, the magnitude of the effective stress cycles experienced by both models in the near-surface will be the same. At greater depth, the numerical model predicts smaller pore water pressure fluctuation than measured. This can be explained by the hydrogeological properties used within the numerical analysis. These give lower hydraulic conductivity at depth than in the physical model due to the relationships employed not accounting for preferential flow routes.

As stipulated previously, this work is interested in validating near-surface behaviour of clay slopes subjected to wetting and drying stress cycles, therefore, it is the near-surface hydrogeological behaviour that is of significance and pore water pressure cycles at depth are of less relevance within this study.

Mechanical Behaviour

494 The hydrogeological behaviour of the physical system and corresponding effective
495 stress cycles within the near-surface of the slopes due to seasonal wetting and
496 drying have been replicated within the numerical analyses. This allows mechanical
497 behaviour of the numerical models driven by these established stress cycles to be
498 compared with the measured deformations from the physical modelling. This is
499 critical in demonstrating and validating that the numerical modelling approach
500 developed can effectively replicate seasonal driven cycles of shrink-swell
501 displacements, seasonal ratcheting, and progressive failure and is a key contribution
502 of this study.

503 Figure 11 shows measured and modelled displacements for WAT7a and
504 demonstrates that the distinctive shrink-swell movement and accumulation of
505 outward and downward displacements, characteristic of seasonal ratcheting, are
506 captured using the approach described in this paper. Key aspects of seasonal
507 ratcheting behaviour have been captured; primarily vertical movement with little
508 horizontal displacement at the crest of the slope and conversely, significant
509 horizontal movement with little vertical displacement at the toe. However, there are
510 larger vertical displacements obtained in the numerical model than the physical
511 model at all locations.

512 The magnitudes of net displacements at the toe and mid-slope are close to those
513 observed experimentally following a complete cycle of wetting and drying (i.e. D-F in
514 Figure 11). In addition, Figure 12 shows that the magnitude of shear strains and
515 areas affected by strain accumulation at the toe of the slope at different times within
516 the analyses are comparable between the physical and numerical model. It should
517 be noted that there are a far greater number of points where strains are calculated
518 within the numerical model compared to the number of measurement points in the

519 physical models, which is why much higher shear strains are seen very close to the
520 toe of the slope. The accumulation of shear strains, a portion of which are elastic and
521 a portion plastic, illustrate the onset of progressive failure and mobilisation of post-
522 peak strength within the slope due to the pore water and hence effective stress
523 cycles experienced and movements that have occurred.

524 The larger vertical displacements observed in the numerical models can be
525 explained by considering how the stress cycles within the near surface have been
526 driven. Boundary conditions have been calibrated to replicate pore water pressure
527 and therefore stress cycles at HCT1, approximately 1.0m depth within the slope
528 model at full scale. From the discussion of hydrogeological response of the
529 numerical model, it was established that the saturated hydraulic conductivity
530 relationship used within the numerical analyses is lower than the physical model.
531 Therefore, considering drying, to achieve the same pore water pressure, and thus
532 stress condition, at 1.0m depth in the numerical model will require a discharge
533 boundary condition that is greater than will be experienced in the physical model.
534 This increased magnitude discharge boundary condition applied along the slope
535 surface will result in greater vertical deformation of points along the slope surface,
536 and it is these surface points that have been used for the comparison of the
537 numerical and physical model. In addition to the differences between the numerical
538 model and physical model boundary conditions, an isotropic stiffness model has
539 been used in the numerical analyses, but it is known that stiffness of consolidated
540 clays is in fact anisotropic. This difference will have contributed to some of the
541 differences observed.

542 Figure 13 shows the void ratios within the numerical analyses after a drying and
543 wetting phase. The stiffness and saturated hydraulic conductivity relationships are a

544 function of void ratio and are therefore stress dependent. It can be seen that there is
545 a significant change in the near-surface void ratio following wetting and swelling of
546 the soil, from a void ratio of around 1.10 at the end of drying increasing to
547 approximately 1.25 at the end of wetting. This variation adds further justification to
548 why material properties (i.e. stiffness and saturated hydraulic conductivity) must be
549 related to stress state.

550 Figure 14 shows a comparison of displacements for model WAT8a. Again, there are
551 greater vertical displacements within the numerical model but the annual cycle of
552 wetting and drying produces movements representative of seasonal ratcheting
553 observed in the physical modelling. Figures 11 and 14 demonstrate that the
554 numerical modelling approach developed can replicate the mechanical behaviour of
555 seasonal ratcheting for slopes with different initial stress conditions.

556 Neither slope model experienced complete failure during the physical modelling.
557 However, small sections at the toe of the slopes became detached from the models
558 at the end of the seasonal cycles imposed. This brittle behaviour following softening
559 observed in the physical model cannot be captured within the numerical model as
560 the soil is assumed to act as a continuum. However, large plastic strains were
561 observed in the toe of the slopes at the end of both numerical analyses.

562 The shear strains within WAT7a at waypoint G and the end of analysis, waypoint H,
563 have been considered in Figure 15. The shear strain contour plots show that there
564 are much higher shear strains and therefore softening within WAT7a following the
565 prolonged wetting at the end of the analysis. Figure 15 demonstrates the significance
566 of a prolonged wet period on the overall condition of a slope. The plot also illustrates
567 the nature of the progressive failure mechanism and the onset of softening from the

toe of the slope propagating back and up into the slope, which is a common observation (Skempton, 1964; Potts, et al., 1997; Leroueil, 2001). The numerical modelling approach developed can capture the mechanism of seasonal ratcheting; characteristic movements due to environmental stress cycles, plastic strain accumulation and progressive failure.

Effects of Stiffness Parameters on Seasonal Ratcheting

Given the validation of the numerical modelling approach presented, the approach has been used to investigate the implication of different stiffness parameters on the mechanical behaviour of seasonal ratcheting. This has been done by considering the material used within the numerical model validation (Material A) and a stiffer material (Material B). Slopes formed of the two materials with the same hydrogeological properties have been subjected to the same continuous seasonal pore water pressure cycles, and therefore effective stress cycles, to failure. The geometry and initial consolidation pressure of model WAT7a have been used with extended cyclic boundary conditions used to drive multiple -40kPa at the end of summer to 0kPa at the end of winter, pore water pressure cycles at the location of HCT1. The stiffness parameters for materials A and B are summarised in Table 3.

The results for the two stiffness soils are shown in Figure 16. For Material B, the seasonal movement caused by the stress cycles is considerably less than that of Material A. The magnitude of plastic deformation in a single wetting and drying cycle is smaller and the time taken for the slope to fail due to mobilisation of post-peak strength is much longer: 32 cycles in comparison to 14 cycles. Failure is defined by sudden acceleration of the failing mass (i.e. significantly increased displacements within a single stress cycle). This demonstrates the importance in using the

592 appropriate stiffness relationship when modelling seasonal-driven behaviour and
593 assessing deterioration due to seasonal ratcheting and progressive failure.

594 Interestingly, the shear bands obtained from the two models experiencing continued
595 seasonal stress cycles are both shallow and only incorporate the toe of the slope
596 (Figure 16f). While the slopes modelled are not directly comparable to high-plasticity
597 clay infrastructure slopes (i.e. having different stress histories, the inclusion of
598 vegetation, material variability etc.) the failure modes predicted by the numerical
599 analyses when considering environmental stress cycles are indicative of failures
600 observed in ageing high-plasticity clay infrastructure slopes (Briggs, et al., 2017).
601 The failures generated in the physical and numerical models and observed in
602 infrastructure slopes due to continued cyclic effective stresses are different to
603 deeper-seated progressive failure modes that result from prolonged wetting and
604 previously modelled by Potts, et al., (1997) and Summersgill, et al., (2017).

605 # Discussion

606 The aim of the work described in this paper was to develop a numerical model
607 capable of capturing seasonal ratcheting behaviour of high-plasticity
608 overconsolidated clay slopes subjected to pore water and hence effective stress
609 cycles driven by wetting and drying. It has been conclusively demonstrated that
610 discharge boundary conditions within a two-phase flow software package that
611 employs Bishop's generalised effective stress can replicate seasonal ratcheting
612 behaviour and progressive failure if a van Genucten (1980) style soil water retention
613 curve and relative hydraulic conductivity function to couple hydrogeological and
614 mechanical behaviour, and a strain-softening constitutive model are employed.

This study considers an idealised uniform high-plasticity overconsolidated soil with simple summer-winter boundary conditions without vegetation. The failure mechanism obtained using the numerical model replicates behaviour observed experimentally. The failures predicted by the numerical analyses are indicative of shallow first-time failures of ageing high-plasticity clay infrastructure slopes (Briggs, et al., 2017). To the best of the authors' knowledge, this is the first time that seasonal ratcheting movements and progressive failure due to wetting and drying stress cycles have been replicated within a numerical framework and validated against measured physical behaviour. The work extends previous published work on deep-seated failure mechanisms (Potts, et al., 1997; Kovacevic, et al., 2001; Nyambayo, et al., 2004) and weather-driven deformations of reactivated natural slope by Conte, et al., (2016).

The presented slope models clearly demonstrate deterioration of high-plasticity clay slopes through shear strain accumulation and progressive failure due to repeated stress cycles driven by wetting and drying. The mechanism explored provides an explanation for why a high-plasticity clay slope experiencing multiple similar seasonal 'wet' conditions can fail due to a 'wet' event with the same magnitude as an event that it had previously experienced and remained stable. With each seasonal stress cycle, the condition of high-plasticity clay slopes can deteriorate, and the magnitude of the final triggering event required to cause failure decreases. High-plasticity clay slope deterioration occurs when near hydrostatic conditions are reached and it is the frequency and duration spent at these conditions that dictates the rate of deterioration. Understanding this deterioration process is vital to the assessment of long-term behaviour of high-plasticity clay infrastructure earthworks, in addition to investigating the implications of climate change.

The significance of stiffness properties on seasonal ratcheting has also been demonstrated. To understand the rate of deterioration of a high-plasticity clay slope adequately and to allow meaningful assessment of performance against number of seasonal stress cycles, the stiffness relationship adopted must be representative of the soil forming the slope.

More rigorous approaches are available for modelling unsaturated soil problems (compared to Bishop's generalised effective stress method adopted in this work), although they require use of a greater number of soil parameters, which may not be practical. However, the validation presented has shown that the approach adopted is capable of replicating and quantifying the observed mechanism of behaviour.

The analyses undertaken within this study utilise a nonlocal strain-softening regulatory model to reduce mesh dependency, the approach used has been presented and investigated extensively by others (i.e. Summersgill, et al., 2017). As such, this work does not aim to improve current modelling capability considering progressive failure.

The work replicates physical modelling of summer drying and winter wetting and to model this numerically, simple uniform wetting and drying discharge boundary conditions have been applied to the numerical analyses. This work validates an approach for modelling the mechanism of seasonal ratcheting but does not progress current approaches for modelling land-climate boundary conditions. The use of a single soil water retention curve to relate suctions and saturations is a simplification. It is known that hysteresis and variation in soil water retention properties due to stress state are important characteristics of behaviour but these have not been included within this study due to a lack of material property data for these aspects.

Conclusion

A numerical modelling framework including unsaturated behaviour and a nonlocal strain-softening regulatory model has been developed to investigate seasonal ratcheting in high-plasticity clay slopes. The numerical modelling approach developed has been subjected to defined wetting and drying stress cycles and the mechanical slope behaviour produced is indicative of seasonal ratcheting displacements (i.e. outward and downward movements) observed in physical modelling. It has been shown that seasonal ratcheting deformations due to repeated wetting and drying stress cycles in high-plasticity clay slopes can lead to plastic strain accumulation and progressive failure resulting in shallow first-time failures.

The validation of the numerical modelling approach against physical modelling results, and parametric study undertaken have shown that strength deterioration of high-plasticity clay slopes due to seasonal wetting and drying stress cycles occurs when near hydrostatic conditions are reached within the near surface of a slope. It is the frequency and duration at which these conditions are reached that dictates the rate of strength deterioration. In addition, a parametric study has shown that material stiffness has a significant influence on the magnitude of seasonal movements occurring due to wetting and drying stress cycles, and hence the rate of deterioration of a high-plasticity clay slope due to progressive failure and mobilisation of post-peak strength.

While enhancements to the modelling framework can still be made (i.e. improved land-climate boundary conditions and inclusion of stiffness anisotropy), this study demonstrates it is possible to capture the role of cyclic wetting and drying behaviour driving progressive failure resulting in shallow first-time failure in high-plasticity clay

slopes. This is an important step in better understanding the mechanism of seasonal ratcheting and delivers the potential to study the implications of climate change on the rate of slope deterioration due to this mechanism.

Acknowledgements

The authors gratefully acknowledge Loughborough University for funding the work presented, the iSMART (EPSRC project EP/K027050/1) and ACHILLES project group (EPSRC programme grant EP/R034575/1) for their support.

References

Almeida, M. S. S., Britto, A. M. and Parry, R. H. G. (1986) Numerical modelling of a centrifuged embankment on soft clay. *Canadian Geotechnical Journal*, 23(2) 103-114. Available from https://doi.org/10.1139/t86-020.

Al-Tabbaa, A. and Wood, D. M. (1987) Some measurements of the permeability of kaolin. *Géotechnique*, 37(4) 499-514. Available from https://doi.org/10.1680/geot.1987.37.4.499.

Bashir, R., Sharma, J. & Stefaniak, H. (2016) Effect of hysteresis of soil-water characteristic curves on infiltration under different climatic conditions. *Canadian Geotechnical Journal,* 53, 273-284. Available from https://doi.org/10.1139/cgj-2015-0004.

Briggs, K. M., Loveridge, F. A. and Glendinning, S. (2017) Failures in transport infrastructure embankments. *Engineering Geology*, 219, 107-117. Available from https://doi.org/10.1016/j.enggeo.2016.07.016.

Cekerevac, C. and Laloui, L. (2004) Experimental study of thermal effects on mechanical behaviour of a clay. *International Journal for Numerical and Analytical Methods in Geomechanics*, 28(3) 209-228. Available from https://doi.org/10.1002/nag.332.

Clegg, D. P. (1981) *Model piles in stiff clay*. PhD Thesis. Cambridge University.

Conte, E., Troncone, A. and Donato, A. (2016) A simple approach for evaluating slope movements induced by groundwater variation. *Procedia Engineering*, 158, 200-205. Available from https://doi.org/10.1016/ j.proeng.2016.08.429.

717 Elia, G., Cotecchia, F., Pedone, G., Vaunat, J., Vardon, P. J., Pereira, C.,
718 Springman, S. M., Rouainia, M., Askarinejad, A., Stirling, R., Helm, P., Lollino, P.
719 and Osinski, P. (2017) Numerical modelling of slope-vegetation-atmosphere
720 interaction: an overview. *Quarterly Journal of Engineering Geology and Hydrology*,
721 50, 249-270. Available from https://doi.org/10.1144/qjegh2016-079.

722 Galavi, V. and Schweiger, H. F. (2010) Nonlocal multilaminate model for strain
723 softening analysis. *International Journal of Geomechanics*, 10(1) 30-44. Available
724 from https://doi.org/10.1061/(ASCE)1532-3641(2010)10:1(30).

725 Hu, R., Chen, Y.-H., Liu, H.-H. and Zhou, C.-B. (2013) A water retention curve and
726 unsaturated hydraulic conductivity model for deformable soils: consideration of the
727 change in pore-size distribution. *Géotechnique*, 63(16) 1389-1405. Available from
728 https://doi.org/10.1680/geot.12.P.182.

729 Hudacsek, P., Bransby, M. F., Hallett, P. D. and Bengough, A. G. (2009) Centrifuge
730 modelling of climatic effects on clay embankments. *Proceedings of the Institution of*
731 *Civil Engineers - Engineering Sustainability*, 162(2) 91-100. Available from
732 https://doi.org/10.1680/ensu.2009.162.2.91.

733 Itasca Consulting Group, Inc. (2011) *FLAC - Fast Lagrangian Analysis of Continua*
734 [software]. Version 7.0. Minneapolis, USA.

735 Jardine, R. J., Gens, A., Hight, D. W. and Coop, M. R. (2004) Developments in
736 Understanding Soil Behaviour. In: *Advances in Geotechnical Engineering: The*
737 *Skempton Conference,* London, UK, 29–31 March. London, UK: Thomas Telford,
738 103-206.

739 Kovacevic, N., Potts, D. M. and Vaughan, P. R. (2001) Progressive failure in clay
740 embankments due to seasonal climate change. In: *Proceedings of the International*
741 *Conference on Soil Mechanics and Geotechnical Engineering,* Istanbul, Turkey, 27-
742 31 August. Lisse, Netherlands: A. A. Balkema, 2127-2130.

743 Leroueil, S. (2001) Natural slopes and cuts: movement and failure mechanisms.
744 *Géotechnique*, 51(3) 197-243. Available from https://doi.org/
745 10.1680/geot.2001.51.3.197.

746 Mayne, P.W. and Kulhawy, F.H. (1982) K0–OCR relationship in soil. *Journal of the*
747 *Geotechnical Engineering Division*, 108 (GT6) 851–872.

748 Nuth, M. and Laloui, L. (2008) Effective stress concept in unsaturated soils:
749 Clarification and validation of a unified framework. *International Journal for*
750 *Numerical and Analytical Methods in Geomechanics*, 32(7) 771-801. Available from
751 https://doi.org/10.1002/nag.645.

752 Nyambayo, V. P., Potts, D. M. and Addenbrooke, T. I. (2004) The influence of
753 permeability on the stability of embankments experiencing seasonal cyclic pore
754 water pressure changes. In: *Advances in Geotechnical Engineering: The Skempton*
755 *Conference,* London, UK, 29–31 March. London, UK: Thomas Telford, 898-910.

756 O'Brien, A. S., Ellis, E. and Russell, D. (2004) Old railway embankment clay fill -
757 laboratory experiments, numerical modelling and field behaviour. In: *Advances in*
758 *Geotechnical Engineering: The Skempton Conference,* London, UK, 29–31 March.
759 London, UK: Thomas Telford, 911-921.

760 Potts, D. M., Dounias, G. T. and Vaughan, P. R. (1990) Finite element analysis of
761 progressive failure of Carsington embankment. *Géotechnique*, 40(1) 79-101.
762 Available from http://doi.org/10.1680/geot.1990.40.1.79.

763 Potts, D. M., Kovacevic, N. and Vaughan, P. R. (1997) Delayed collapse of cut
764 slopes in stiff clay. *Géotechnique*, 47(5) 953-982. Available from
765 https://doi.org/10.1680/geot.1997.47.5.953.

766 Rouainia, M., Davis, O., O'Brien, T. and Glendinning, S. (2009) Numerical modelling
767 of climate effects on slope stability. *Proceedings of the Institution of Civil Engineers -*
768 *Engineering Sustainability*, 162(2) 81-89. Available from
769 https://doi.org/10.1680/ensu.2009.162.2.81.

770 Schofield, A. and Wroth, P. (1968) *Critical state soil mechanics*. London, UK:
771 McGraw-Hill.

772 Skempton, A. W. (1964) Long-term stability of clay slopes. *Géotechnique*, 14(2) 77-
773 101. Available from https://doi.org/10.1680/geot.1964.14.2.77.

774 Smethurst, J. A., Clarke, D. and Powrie, W. (2012) Factors controlling the seasonal
775 variation in soil water content and pore water pressures within a lightly vegetated
776 slope. *Géotechnique*, 62(5) 429-446. Available from
777 https://doi.org/10.1680/geot.10.P.097.

778 Smethurst, J., Clarke, D. & Powrie, W. (2006) Seasonal changes in pore water
779 pressure in a grass-covered cut slope in London Clay. *Géotechnique*, 56(8) 523-537.
780 Available from https://doi.org/10.1680/geot.2006.56.8.523.

781 Summersgill, F. C. (2015) *Numerical modelling of stiff clay cut slopes with nonlocal*
782 *strain regularisation*. PhD Thesis. Imperial College.

783 Summersgill, F. C., Kontoe, S. and Potts, D. M. (2017) On the use of nonlocal
784 regularisation in slope stability problems. *Computers and Geotechnics*, 82, 187-200.
785 Available from https://doi.org/10.1016/j.compgeo.2016.10.016.

786 Take, W. A. (2003) *The influence of seasonal moisture cycles on clay slopes*. PhD
787 Thesis. University of Cambridge.

788 Take, W. A. & Bolton, M. D. (2002) An atmospheric chamber for the investigation of
789 the effect of seasonal moisture changes on clay slopes. In: *Proceedings of the*
790 *International Conference on Physical Modelling in Geotechnics (ICPMG02).*
791 Rotterdam: Balkema, 765-770.

792 Take, W. A. and Bolton, M. D. (2003) Tensiometer saturation and reliable
793 measurement of matric suction. *Géotechnique*, 53(2), pp. 159-172. Available from
794 https://doi.org/10.1680/geot.2003.53.2.159.

795 Take, W. A. and Bolton, M. D. (2004) Identification of seasonal slope behaviour
796 mechanisms from centrifuge case study. In: *Advances in Geotechnical Engineering:*
797 *The Skempton Conference,* London, UK, 29–31 March. London, UK: Thomas
798 Telford, 992-1004.

799 Take, W. A. & Bolton, M. D. (2011) Seasonal ratcheting and softening in clay slopes,
800 leading to first time failure. *Géotechnique*, 61(9) 757-769. Available from
801 https://doi.org/10.1680/geot.9.P.125.

802 Tarantino, A. (2009) A water retention model for deformable soils. *Géotechnique*,
803 59(9) 751-762. Available from https://doi.org/10.1680/ geot.7.00118.

804 Tripathy, S., Tadza, M. Y. M. and Thomas, H. R. (2014) Soil-water characteristic
805 curves of clay. *Canadian Geotechnical Journal*, 51(8) 869-883. Available from
806 https://doi.org/10.1139/cgj-2013-0089.

807 Tsiampousi, A., Zdravkovic, L. and Potts, D. M. (2017) A numerical study of the
808 effect of soil-atmosphere interaction on the stability and serviceability of cut slopes in
809 London Clay. *Canadian Geotechnical Journal*, 54(3) 405-418. Available
810 from https://doi.org/10.1139/cgj-2016-0319.

811 van Genuchten, M. (1980) A closed-form equation for predicting the hydraulic
812 conductivity of unsaturated soils. *Soil Science Society of America Journal*, 44(5) 892-
813 898.

814 White, D. J., Take, W. A. and Bolton, M. D. (2003) Soil deformation measurement
815 using particle image velocimetry (PIV) and photogrammetry. *Géotechnique*, 53(7)
816 619-631. Available from https://doi.org/10.1680/ geot.2003.53.7.619.

817 Wood, D. M. (2004) *Geotechnical Modelling*. London: Spon Press.

Tables

Table 1 Kaolin mechanical properties

Peak Local Strain	0.05
Critical State Local Strain	0.15
Peak Nonlocal Strain	0.05
Critical State Nonlocal Strain	0.15
Internal Length Parameter (m)	0.5
Peak Cohesion (kPa)	6.25
Critical State Cohesion (kPa)	0.00
Peak Friction (º)	24.0
Critical State Friction (º)	24.0
Angle of Dilation (°)	0.0
Unit weight (kN/m^2)	17.9
λ	0.25
κ	0.05
Poisson's Ratio, v'	0.35

Table 2 Fitted van Genuchten Parameters for Kaolin

van Genuchten fitting parameter (kPa)	α	7000
van Genuchten fitting parameter	n	1.85
van Genuchten fitting parameter	m	0.459

Table 3 Stiffness parameters for different materials

	Γ	λ	κ	K_{min} (kPa)
Material A	3.55	0.25	0.05	2000
Material B	2.65	0.124	0.02	3500

Figures

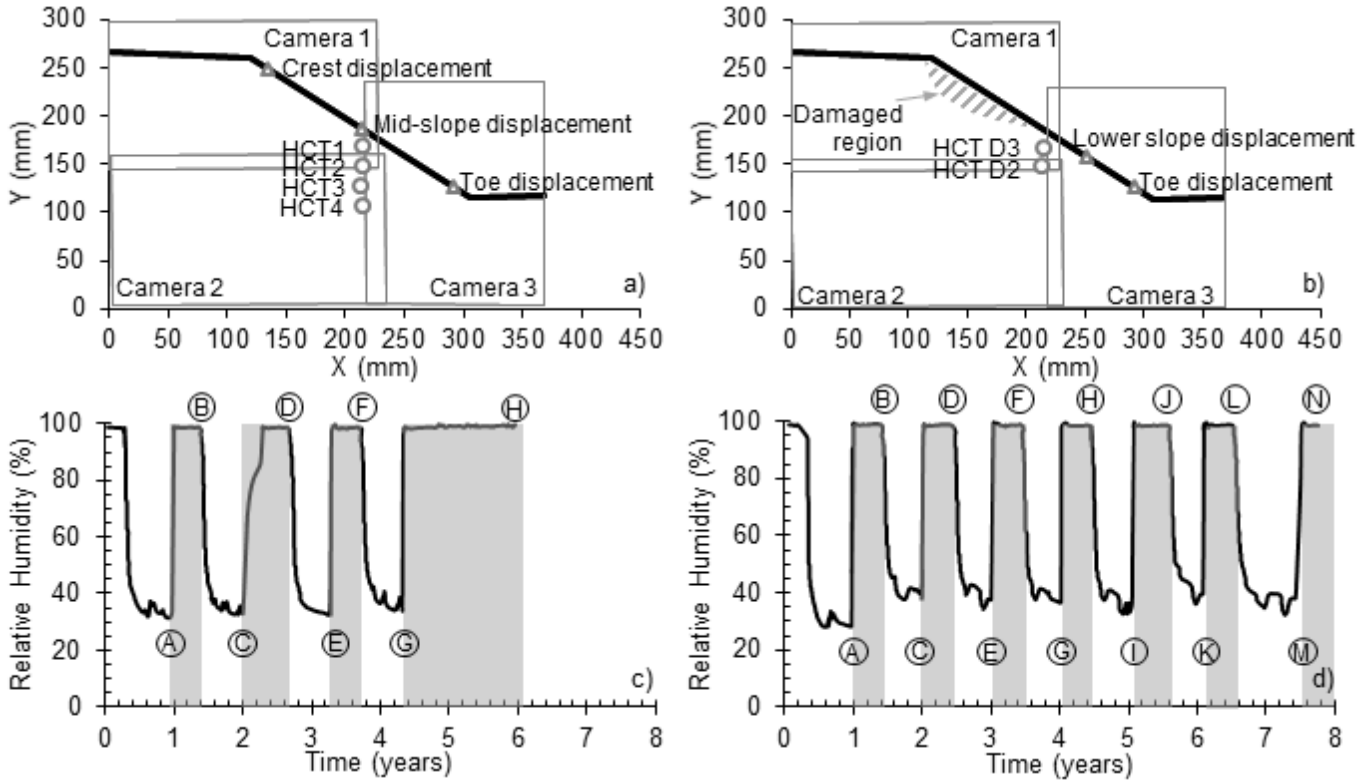

Figure 1 Physical model geometries (at 1/60th scale), camera locations for PIV measurements, tensiometer locations for pore pressure measurements and boundary conditions (after, Take, 2003); a) physical model WAT7a; b) physical model WAT8a; c) WAT7a boundary conditions; d) WAT8a boundary conditions

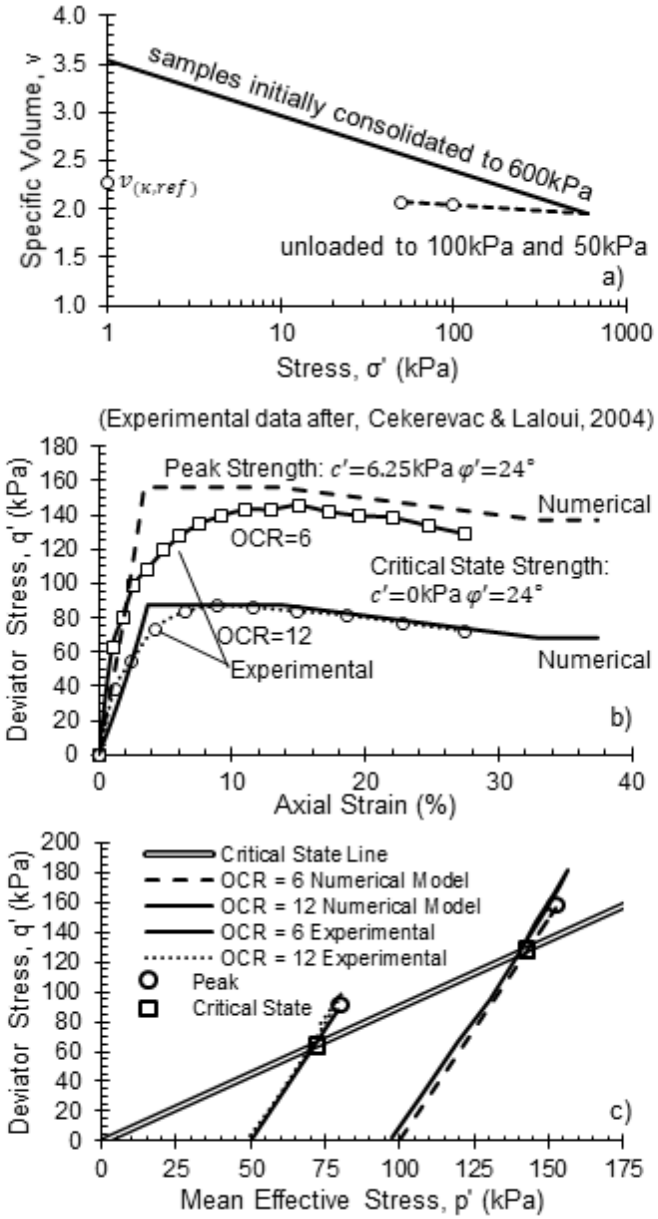

Figure 2 Comparison of measured and modelled triaxial test response of Kaolin (experimental data after, Cekerevac & Laloui, 2004); a) specific volume plot; b) stress-strain plot; c) stress path plot

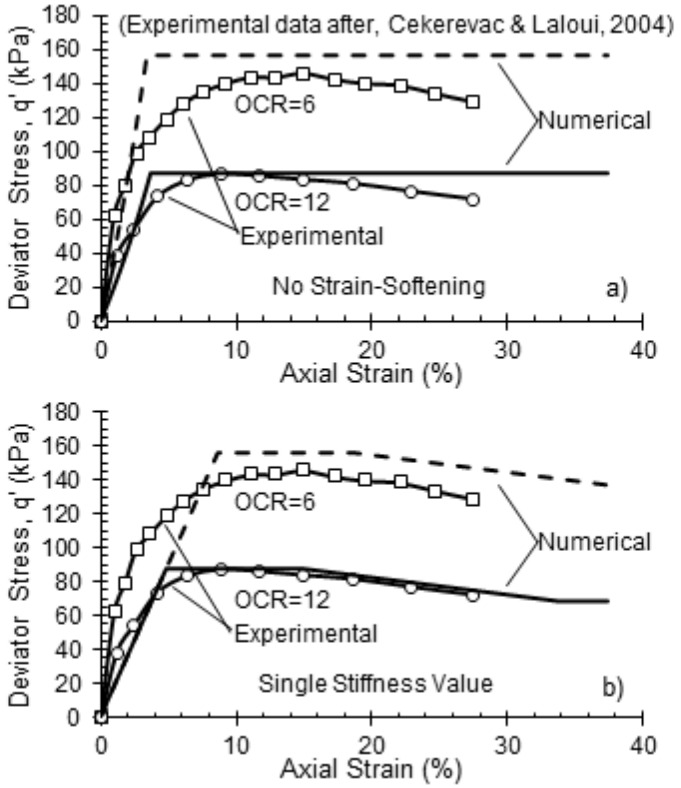

833 Figure 3 Sensitivity analyses of mechanical behaviour of Kaolin – stress-strain plots
834 (experimental data after, Cekerevac & Laloui, 2004); a) no strain-softening
835 behaviour; b) simple stiffness relationship

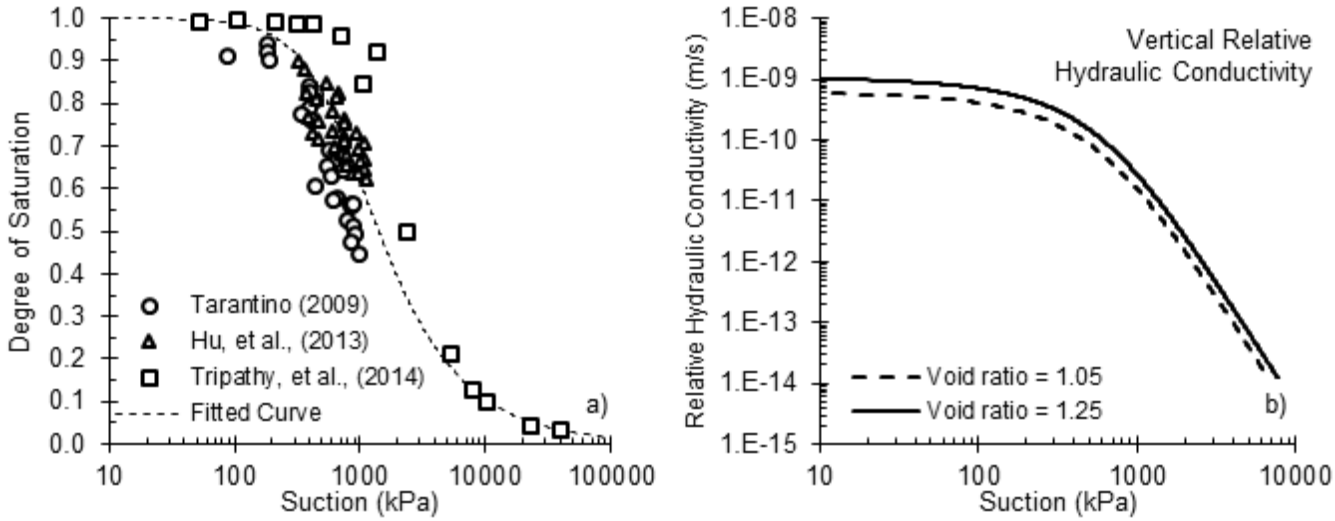

836 Figure 4 Kaolin soil water retention properties; a) soil water retention curve fitted
837 against experimental data (experimental data after, Tarantino, 2009; Hu, *et al*., 2013;
838 Tripathy, *et al*., 2014); b) vertical relative hydraulic conductivity function for different
839 void ratios (*e*)

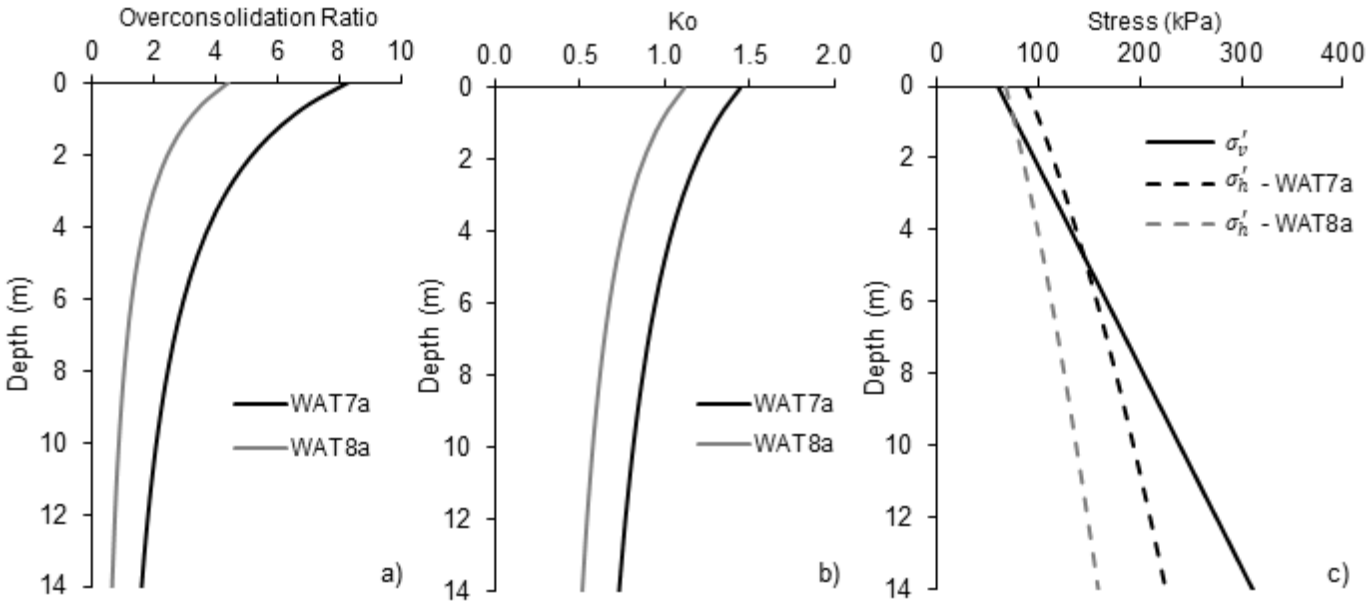

840 Figure 5 Initial stress conditions against depth prior to forming of slopes for WAT7a
841 and WAT8a; a) overconsolidation ratio; b) K_0; c) stress state

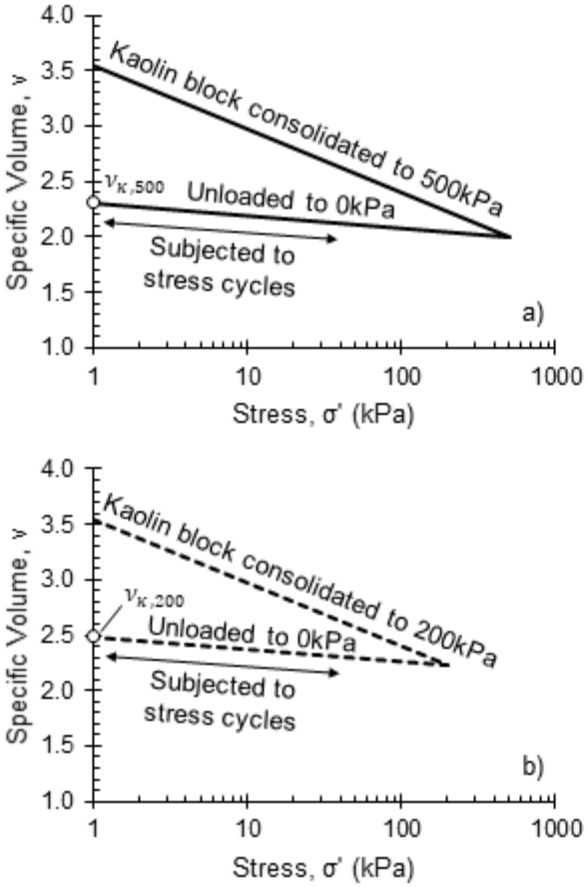

842 Figure 6 Specific volume relationships; a) WAT7a; b) WAT8a

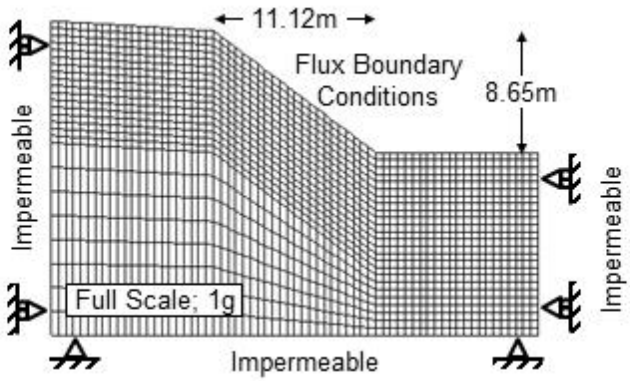

843 Figure 7 Typical mesh used

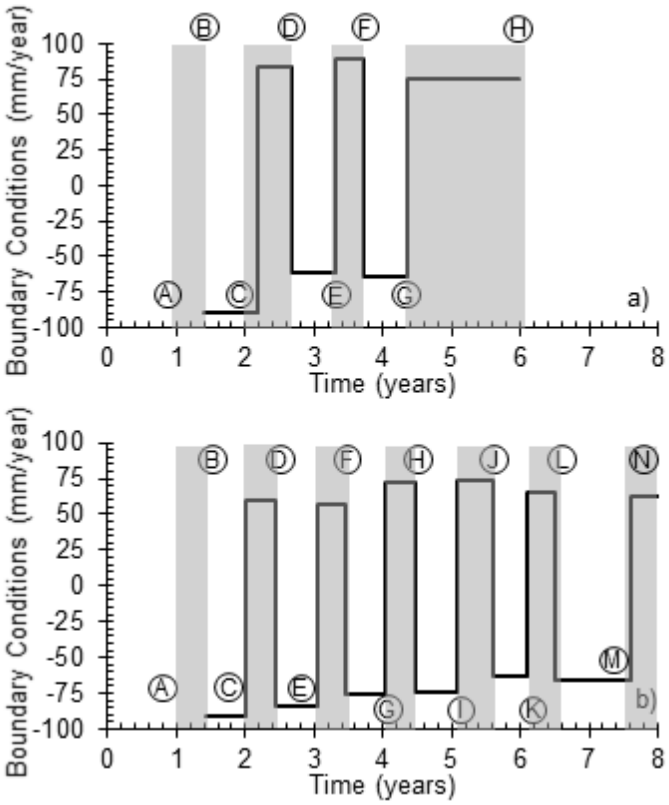

844 Figure 8 Numerical model discharge boundary conditions; a) WAT7a boundary
845 conditions; b) WAT8a boundary conditions

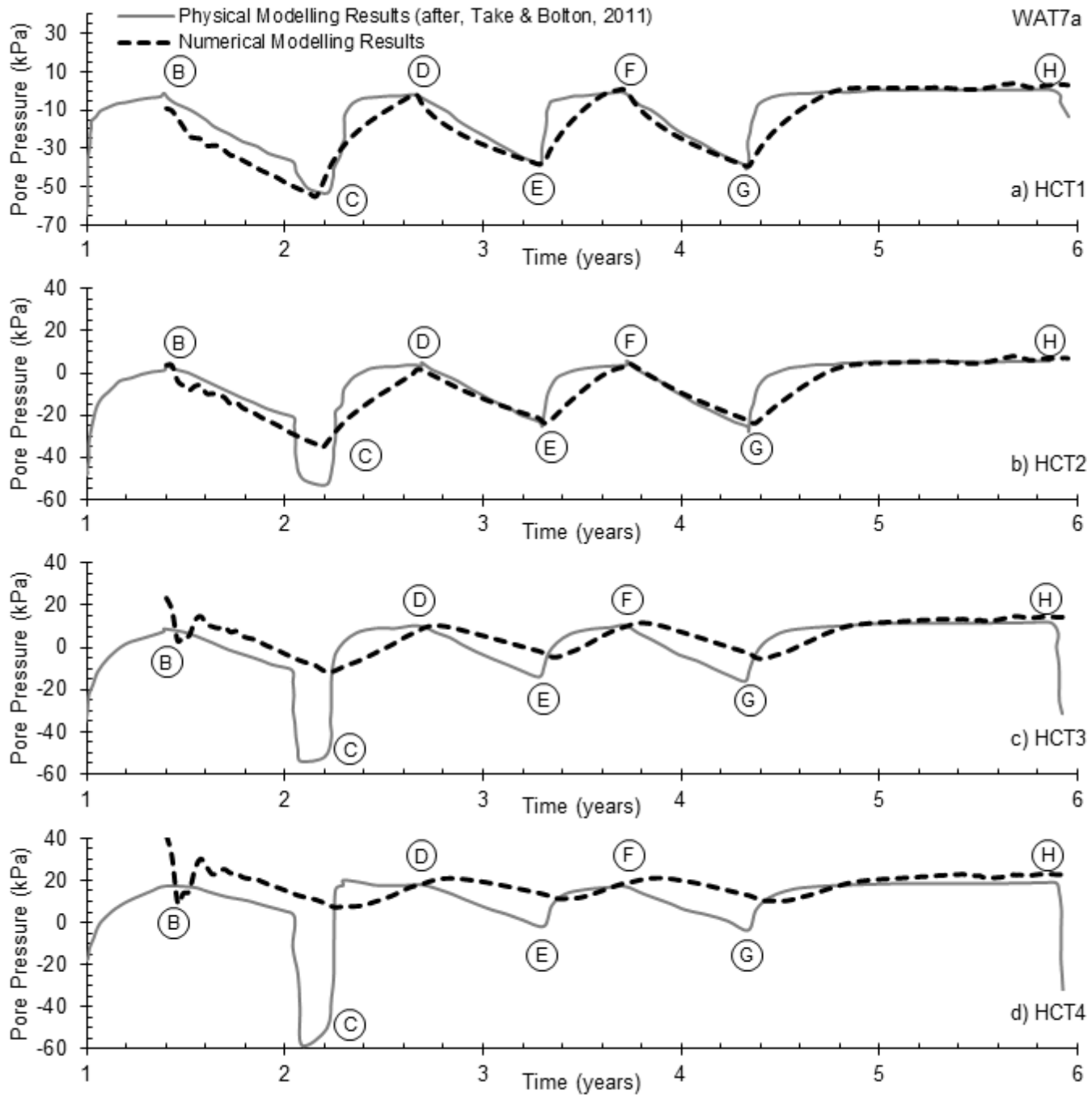

846 Figure 9 Comparison of physical and numerical modelling pore water pressures –
847 WAT7a (experimental data after, Take & Bolton, 2011); a) HCT 1; b) HCT 2; c) HCT
848 3; d) HCT 4

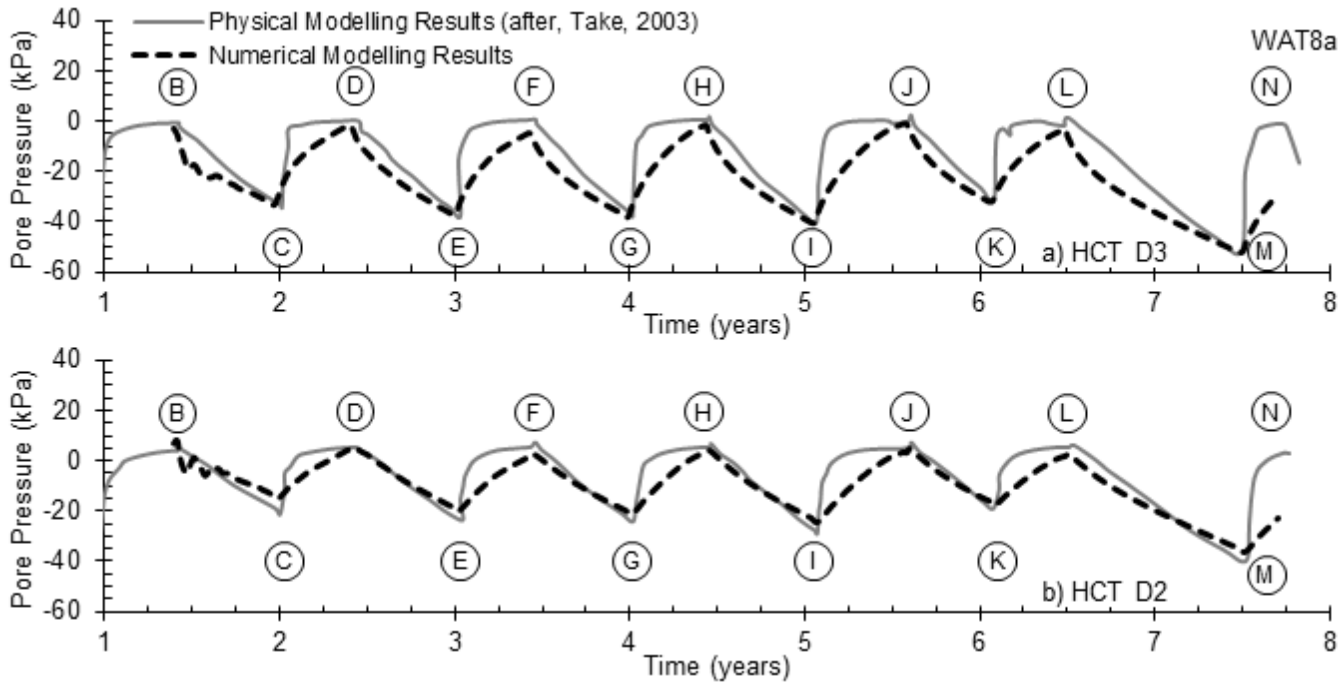

849 Figure 10 Comparison of physical and numerical modelling pore water pressures –
850 WAT8a (experimental data after, Take, 2003); a) HCT D3; b) HCT D2

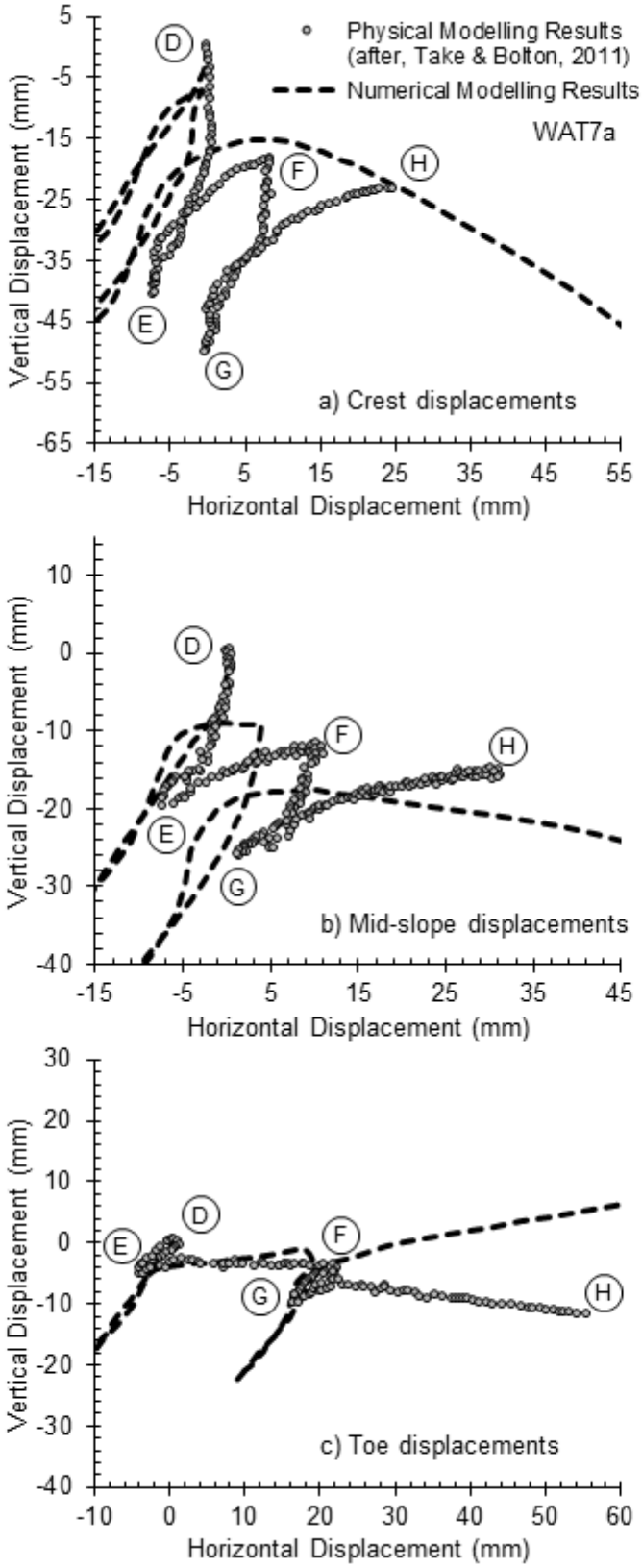

851 Figure 11 Comparison of physical and numerical modelling mechanical behaviour –
852 WAT7a (experimental data after, Take & Bolton, 2011); a) crest displacements; b)
853 mid-slope displacements; c) toe displacements

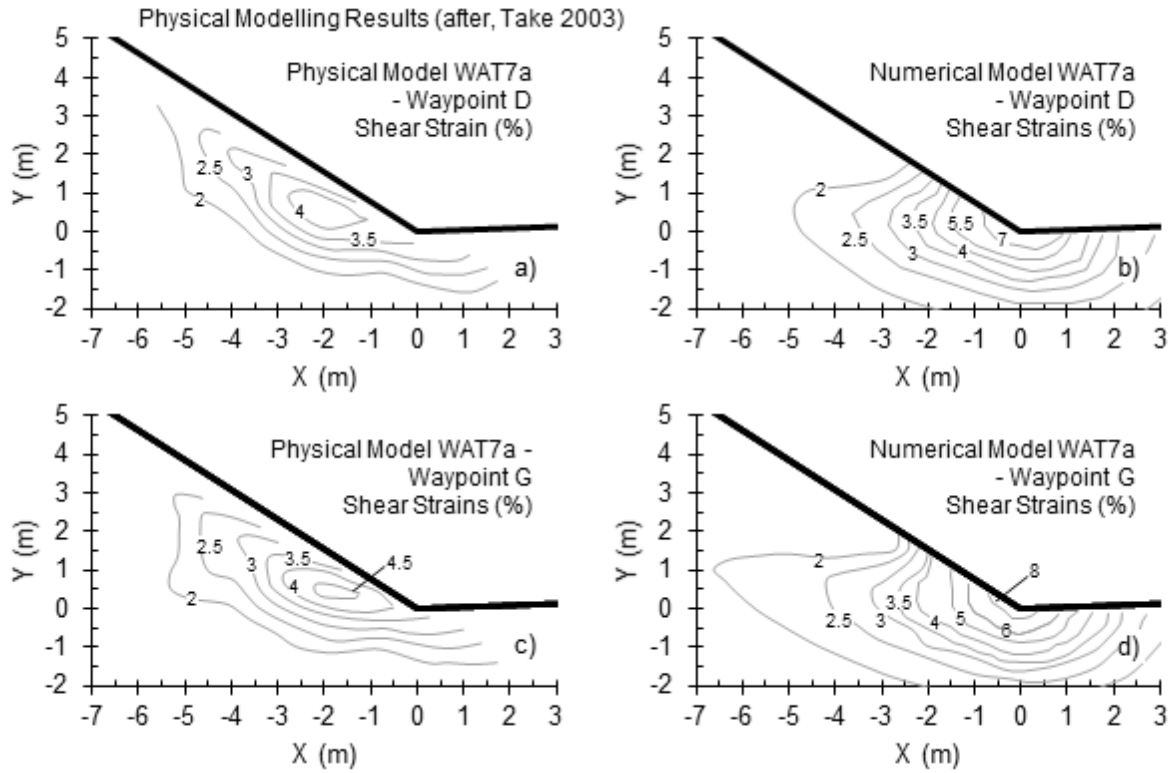

854 Figure 12 Comparison of physical and numerical modelling shear strains – WAT7a
855 (experimental data after, Take, 2003); a) physical modelling waypoint D; b)
856 numerical modelling waypoint D; c) physical modelling waypoint G; d) numerical
857 modelling waypoint G

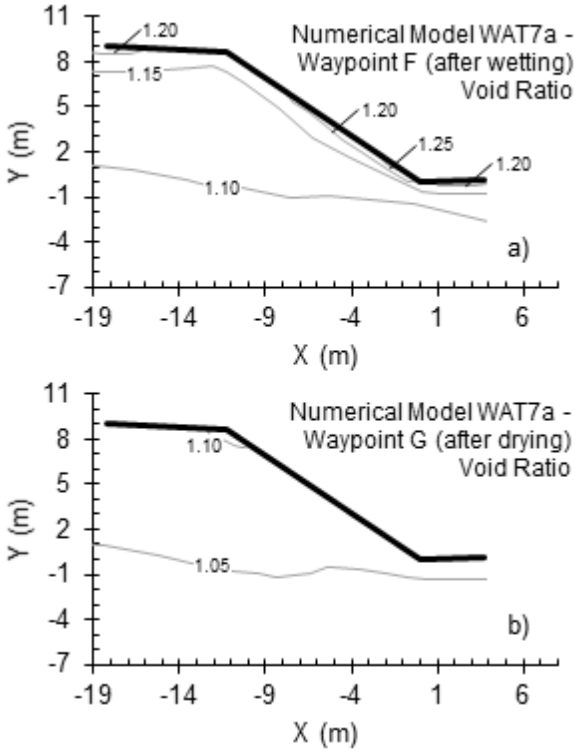

858 Figure 13 Comparison of void ratios within numerical model at different times –
859 WAT7a; a) after wetting – waypoint F; b) after drying – waypoint G

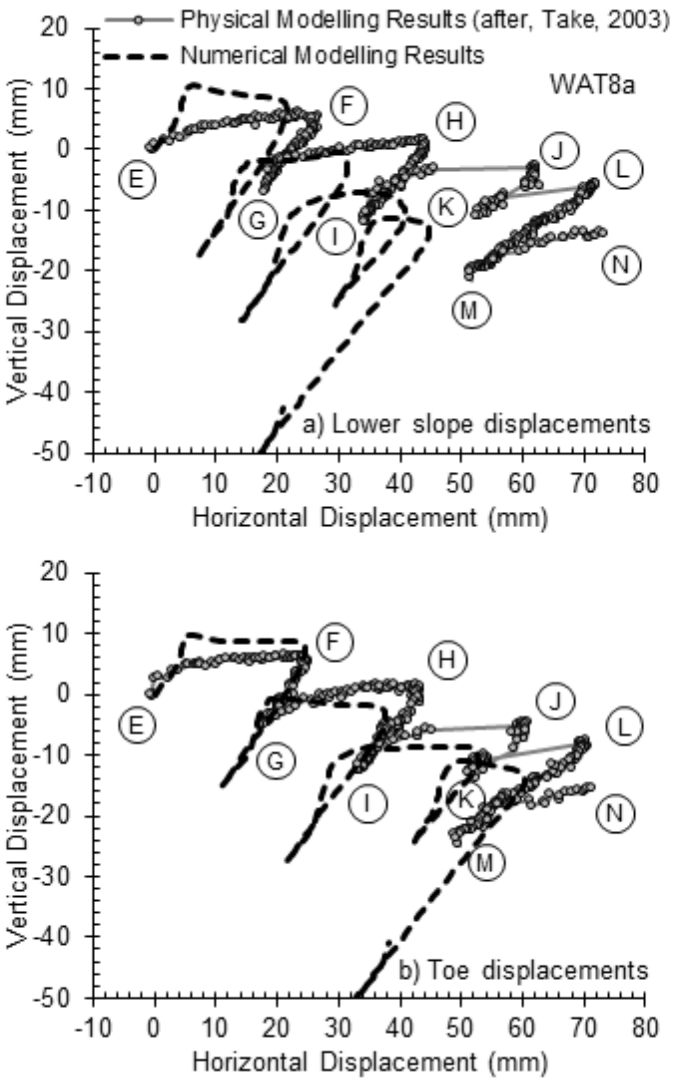

860 Figure 14 Comparison of physical and numerical modelling mechanical behaviour –
861 WAT8a (experimental data after, Take, 2003); a) lower slope displacements; b) toe
862 displacements

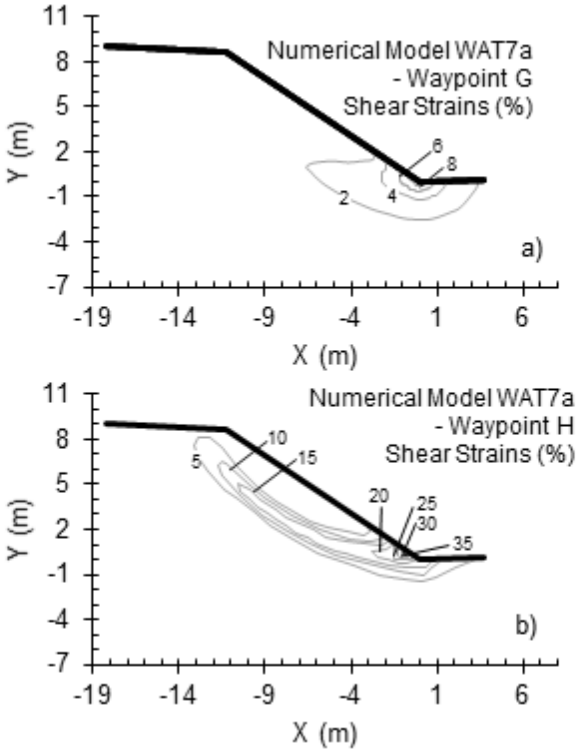

863 Figure 15 Shear strain contours at different points in WAT7a numerical analysis; a)
864 waypoint G; b) waypoint H

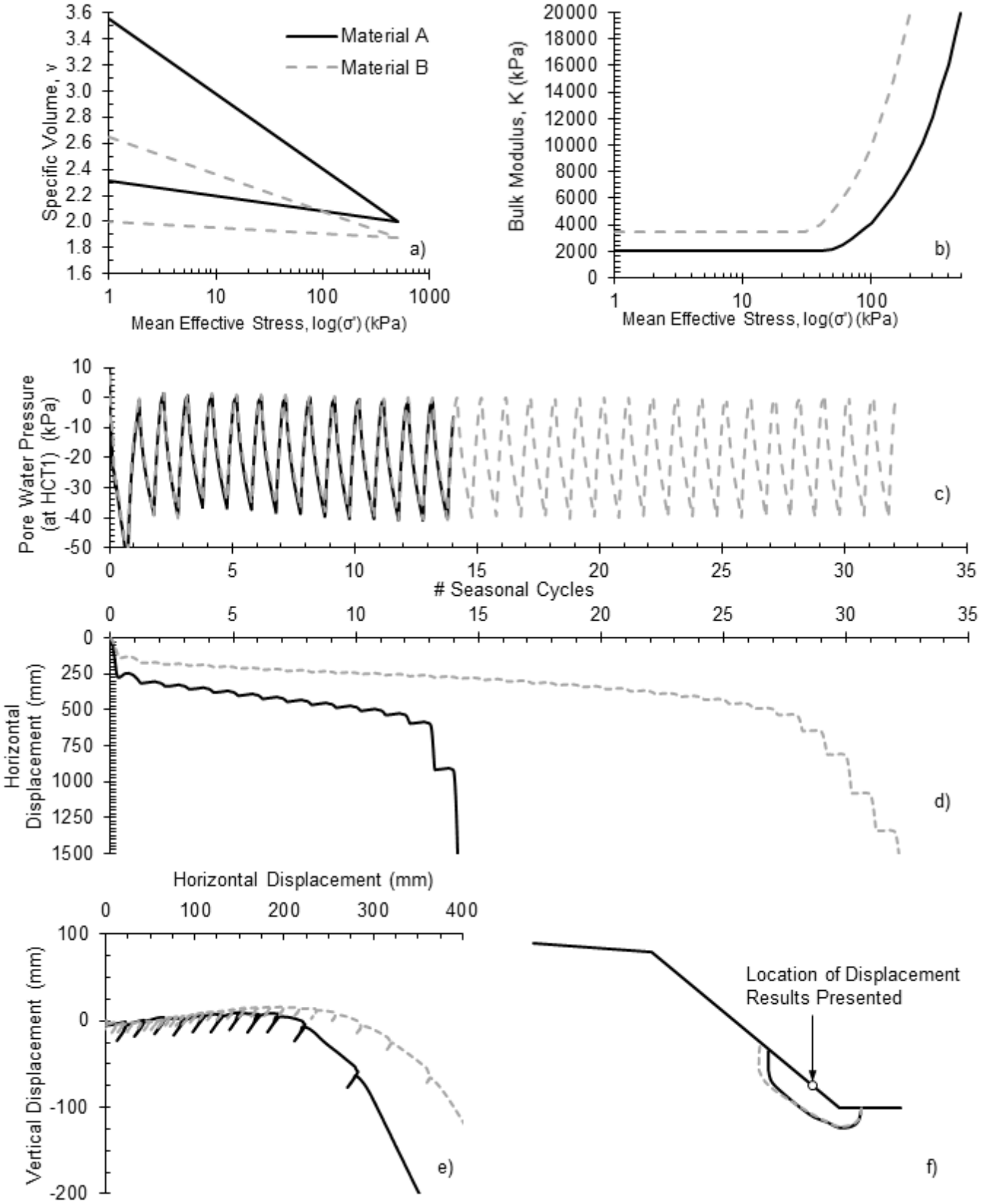

865 Figure 16 Comparison of materials with different stiffness under continued seasonal
866 cycles of wetting and drying; a) specific volume; b) bulk modulus; c) pore water
867 pressure cycles at HCT1; d) horizontal displacements; e) seasonal ratcheting
868 displacements; f) shear surfaces